博士論文 (要約)

Investigation of Bloch surface waves on dielectric multilayers for photonic applications

（フォトニック応用のための誘電体多層膜におけるブロッホ表面波の研究）

鄧志宗

Abstract

The surface wave-based applications have received great attention for their various optical properties and possibilities. Surface plasmon polariton (SPP) is one type of surface wave that can be excited at the interface between metal medium and dielectric medium. SPP has been investigated in a large variety of applications including biosensors, chemical sensors, microscopy, logic gate, and light switching. However, SPP-based applications are intrinsically limited in their practicality by severe ohmic losses occurring in their metal medium. The issue of short propagation lengths, limited operating wavelength, and narrow resonance prevent it from being used as part of the integrated photonic circuit (PIC). PIC offers significant advantages over electronic circuits, such as low-loss information transport and faster information processing.

Bloch surface wave (BSW), as another type of electromagnetic surface wave, BSWs propagate at the interface between a dielectric multilayer and the dielectric medium and are considered to be a dielectric analog to SPPs. BSW-based devices could circumvent the issues of SPP-based devices due to the low-loss propagation and wide operating wavelength regions owing to the metal-free structure. BSW has drawn a great deal of attention and has been studied widely for various applications including sensors, photodetectors, Mach−Zehnder interferometers, and components of photonic integrated circuitry in recent years. However, most of the studies of BSW focus on sensing applications, the study of on-chip integration photonic applications based on BSW are incomplete. The BSW-based on-chip integration photonic applications are promising for the development of low-loss and wide operating wavelength regions PIC.

To realized the BSW-based on-chip integration photonic applications, the manipulation of BSW on a chip is needed. The basic and important components, coupler and guiding slab

are required for the manipulation of BSW. While the coupling of BSW by the grating coupler and the guiding of BSW by guiding-slab has been demonstrated in recent years, the demonstration of the integration of BSW-based grating coupler and guiding-slab is missing. In this study, the integration of BSW-based grating coupler and guiding-slab has been demonstrated, which opens the new possibility of BSW-based on-chip integration photonic applications. Furthermore, the sensing application based on the slab-guided BSW has been demonstrated in this study. Using metal-free structures that can serve as an efficient optical circuit with a long propagation length on a chip opens the new possibilities of the surface wave-based biosensor. This study will impact the development of analysis tools for label-free sensing for use in medical diagnostics, pharmaceutical research, and biological research.

Based on the slab-guided BSW, the all-optical logic gate has been proposed in this study. The all-optical logic gate devices have attracted enormous attention because of their critical applications in the fields of information processes and the development of PIC. There are various approaches to realize the all-optical logic gates such as the formation of constructive/destructive interference in the photonic-crystal structure and the guided-SPP. Although several types of logic gates are realized based on the photonic-crystal structure platform, the intrinsic instability and low extinction ratio between on and off-state hamper it to be used to build a practical photonic circuit. Though the SPP-based all-optical logic gate can overcome the issue of low extinction ratio, the intrinsic ohmic losses from electronic excitation in their metal medium have been seen as a bottleneck for building a practical photonic/plasmonic integrated circuit with low propagation loss. The proposed slab-guided BSW-based logic gate overcomes the issues of photonic-crystal-based and SPP-based all-optical logic gate. In this study, taking advantage of the metal-free structure and BSW interference-based mechanism, the proposed all-optical logic gate can be operated in

telecommunication wavelengths with a high extinction ratio. Moreover, the long-distance waveguide-to-waveguide coupling is reached with a 100 um separation between two waveguides, which is almost 3 orders longer than that of the traditional evanescent waveguide-to-waveguide coupling with around a 250 nm separation has been demonstrated in this study.

The other application based on slab-guided BSW, light switching, has also been demonstrated in this study. As PICs include more individual optical elements and realize more complex functions, the ability to control the propagation direction of light is becoming important. Light switching based on spin-controlled unidirectional coupling has been demonstrated in chiral photonic circuits and SPP-based chiral-metasurface. Chiral-sensitive metasurface, as two-dimensional nanostructures composed of subwavelength elements that can arbitrarily control the propagation direction of electromagnetic waves through spin-controlled coupling, have drawn a lot of attention owing to its high directional selectivity. The ability to control the propagation direction and the operating wavelength of such structures through their shape and period makes them highly flexible. They, therefore, have the potential to facilitate the development of complex optical systems and PICs. However, the BSW-based chiral metasurface has not been demonstrated yet. In this study, the light switching based on BSW-based chiral metasurface has been demonstrated with high directional selectivity and long propagation length at telecommunication wavelengths. The ability to realize light switching on a chip at telecommunications wavelengths using the metal-free chiral-sensitive metasurface makes it promising for applications in low-loss on-chip photonic integrated devices and sensors.

The BSW-based applications have been widely studied as mention. However, most of these BSW platforms require a large number of layers to realize the coupling of the surface mode due to the small difference of refractive index between high- and low-refractive-index material. Additionally, although BSW modes have been investigated in the visible region and

the near-infrared region, very limited reports are available for the mid-infrared region. MIR spectroscopy enables the determination of characteristic vibrational resonances of many functional molecules so that it can be used to perform label-free sensing, medical diagnostics, and food analysis. In this study, the BSW has been demonstrated both in NIR and MIR regions with the Ge/SiO_2 dielectric multilayer by adjusting the thickness of the dielectric layers of the BSW platform. The BSW mode was observed in the MIR range, thus greatly extending the range of BSW wavelengths and possibly reaching the fingerprint region of organic molecules.

Acknowledgements

Contents

List of Figures

List of Tables

Chapter 1 : Introduction

1.1 Background of electromagnetic surface wave

Surface waves occur at the interface between two different media with different types of permittivity or permeability. Owing to the special properties of a surface wave such as field localization and surface sensitivity, the surface waves have attracted a significant amount of attention [1,2]. Surface plasmon polariton (SPP) is one type of surface wave that can be excited at the interface between a metal layer and a dielectric layer [3,4]. The electric field of an SPP is maximum at the interface and decays exponentially in the dielectric layer as well as the metal layer. In order to excite the TM-polarized SPPs, the wave vector of incident light should match with the wave vector of SPPs. From Maxwell's equations, the propagation constant of the surface plasmon wave propagating along the metal-dielectric interface can be expressed as [5]:

$$k_{SPP} = \frac{2\pi}{\lambda}\sqrt{\frac{\varepsilon_m \varepsilon_d}{\varepsilon_m + \varepsilon_d}}$$

where k_{SPP} is the propagation constant of surface plasmon wave, λ is the wavelength of the incident light in free space, ε_m and ε_d are the dielectric constants of metal and dielectric medium which are functions of the wavelength. Prism coupling configuration and grating coupler are two common approaches to enable the wave vector of incident light to match the wave vector of SPPs. In order to excite the SPPs by using prism coupling configuration, the propagation constant of the evanescent wave needs to match the wave vector of SPPs. The evanescent wave is generated by the total internal reflection when the incident light is greater than the critical angle. When the wave vectors are matched, the SPPs will be excited by evanescent waves and propagate along with the interface between the dielectric layer and metal layer as shown in Figure 1-1

(a) and (c). In the case of grating coupler-based coupling, one of the directions of the diffraction of light that generated by incident light along the plane of the grating with a wave vector greater than the wave vector of SPPs. The SPPs will be excited when the matching condition is realized shown in Figure 1-1(c). The matching condition can be realized with a specific period of the grating coupler. The schematic diagram of the SPPs excited by the mean of the grating coupler is shown in Figure 1-1 (b)

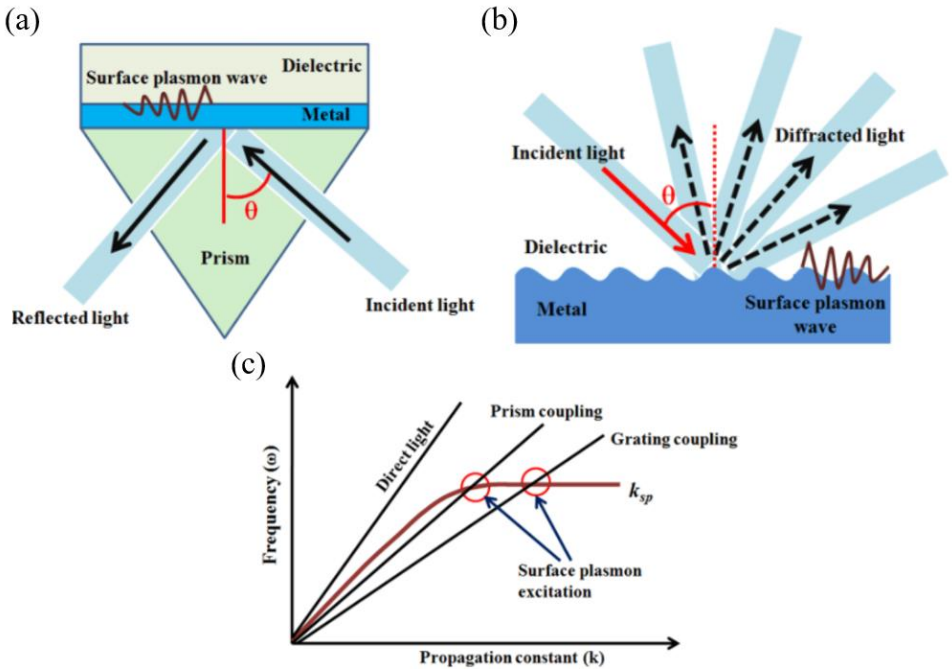

Figure 1-1 The schematic diagram of (a) prism and (b) grating coupler coupling configurations for SPPs excitations. (c) The dispersion curves of surface plasmon wave, the prism coupling, and grating coupler coupling configurations. [5]

In the past decades, SPPs have been investigated in a large variety of applications including biosensors [6,7], chemical sensors [6] [8], microscopy [9], and waveguides [10]. However, SPPs are intrinsically limited by severe ohmic losses occurring in the metal layer so that applications requiring long propagation lengths and/or high-quality resonances have been hampered [11,12]. The propagation length of SPPs L_{SPP} is defined as the distance for the SPW intensity to decay by a factor of 1/e as:

$$L_{SPW} \approx \sqrt{\frac{\varepsilon_1' + \varepsilon_2}{\varepsilon_1'\varepsilon_2}} \frac{\varepsilon_1'(\varepsilon_1' + \varepsilon_2)}{\varepsilon_1''\varepsilon_2} \frac{\lambda}{2\pi}$$

where ε_1' and ε_1'' are the real and imaginary parts of the dielectric function of the metal, respectively. The large value of the imaginary part of refractive index ε_1'' of metal causes the intrinsic short propagation length of SPPs. Therefore, the propagation length of SPPs is limited in the order of tens μm. Figure 1-2 shows the typical propagation behavior of SPPs with waveguides. The light intensity of out-couple light is greatly decreased with the increase of the length of the waveguide. The typical propagation length of SPPs is the order of tens μm.

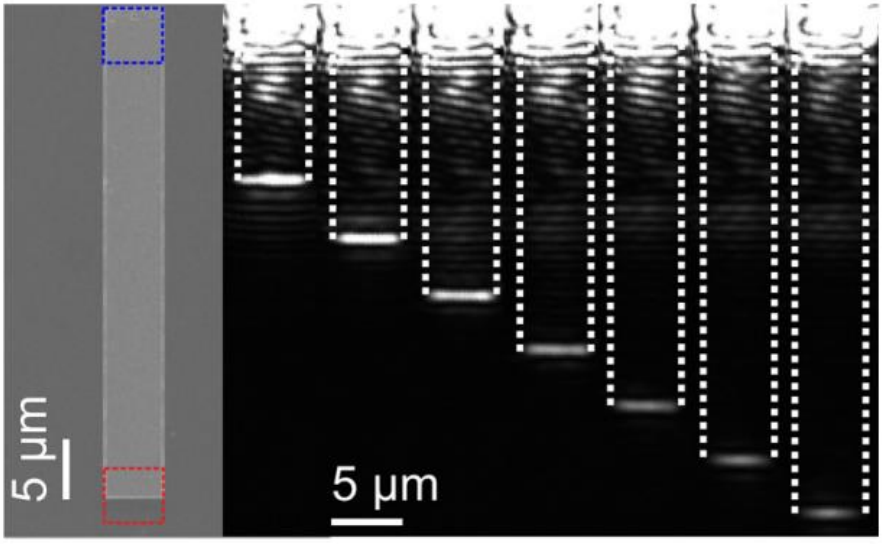

Figure 1-2 Scanning electron microscope (SEM) images of a 5 μm wide and 45 μm long waveguide, and a set of images obtained using a CCD camera. (i) 5 μm wide and 15 μm long waveguide to (vii) 5 μm wide and 45 lm long waveguide [12].

1.2 Bloch surface wave

Bloch surface wave (BSW) is a different type of surface wave that can propagate at the interface between a one-dimensional photonic crystal (1D-PC) and a dielectric medium [13,14]. BSW is considered as the alternative to SPPs due to their superior properties such as longer propagation lengths and wide wavelength range operations [15,16]. While both SPPs and BSWs offer significant electromagnetic field

enhancements at the surface, the mechanisms for the electromagnetic field confinement at the surface are different. In the case of SPPs, the confinement is achieved through the collective oscillations of the free electrons in the metal. These electron oscillations limit the quality of the resonance due to ohmic losses so that the full width at half maximum (FWHM) of the SPP resonances cannot be reduced below some limit that prevents high-resolution spectroscopy. In contrast, BSWs do not require metal layers and support evanescent waves between 1D-PC (dielectric multilayer) and a dielectric medium. Hence, BSWs possess much lower losses than SPPs [14]. The prism coupling configuration and grating coupler coupling that is used in coupling SPPs can also use to couple light into BSW. Figure 1-3(a) shows the schematic of the prism coupling configuration for BSW excitation. When the incident light with a certain wavelength and incident angle that match the wave vector of BSW, the BSW will be excited and propagate at the interface between the dielectric medium (air) and dielectric multilayer. The evanescent decaying normalized electric field distribution in the dielectric multilayer BSW platform (Figure 1-3(b)) shows a typical BSW mode.

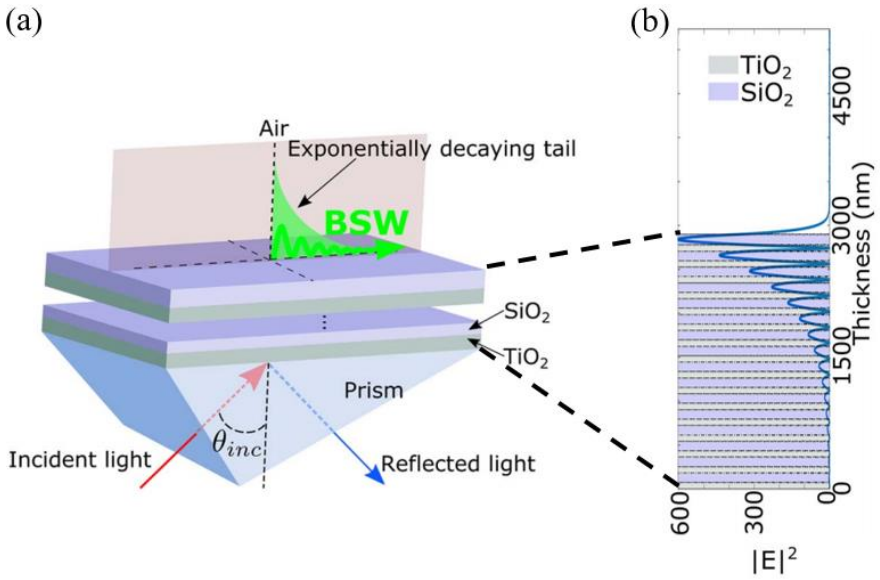

Figure 1-3 (a) Schematic of a prism coupling configuration to excite BSW using a dielectric multilayer. (b) E-field intensity at the surface of a TiO_2/SiO_2 multilayer BSW platform when incident light couple into BSW [17].

Propagation length of BSW L_{BSW} is the distance where the intensity of the propagating field drops down exponentially ($e^{(-y/L_{BSW})}$) to 1/e of its maximum value. The study of the propagation length of BSW at telecommunication wavelength is shown in Figure 1.4. By using the prism coupling approach, BSW is coupled and propagates on the top surface. A fiber probe is used to scan the top surface for observing the propagation of BSW as shown in Figure 1-4(a). Figure 1-4 (b) shows the near-field scanning optical microscope image, which shows the propagation of BSW on the top surface. The field intensity is decreased very slightly with the propagation of BSW, which shows the very low-loss propagation behavior. Figure 1-4(c) shows the exponential fit of the field intensity along the direction of propagation to measure the propagation length. Unlike the metal layer in the SPP platform, there is no metal layer in the BSW platform. Therefore, the propagation length of BSW is much longer than that of SPP. The very long propagation length of BSW with the order of mm at telecommunication wavelengths has been demonstrated with SiN_3/SiO_2 multilayer with a TiO_2 additional

layer as shown in Figure1-4 [18]. The losses of BSW from the (1) absorption in the material, (2) surface scattering, and (3) leakage into the substrate. The absorption in the material can be very low when the low absorption material is used. The surface scattering issued can be largely improved by using high-quality deposition techniques such as plasma-enhanced chemical vapor deposition to realized extremely low loss from surface scattering from the roughness of deposited material [19]. The losses of BSW mainly from the leakage into the substrate. This issue can be improved by increasing the number of layers of the dielectric multilayer. In addition to that, the operating wavelength range of BSW is much wider than that of SPP (mostly in the visible region due to high absorption in the wavelength range above visible region wavelength). Thanks to the large number of possibilities of dielectric material that can be used as the dielectric layer of the BSW platform, the operating wavelength range of BSW is very broad. The BSW in the visible region, near-infrared (NIR) region and mid-infrared (MIR) region have been demonstrated.

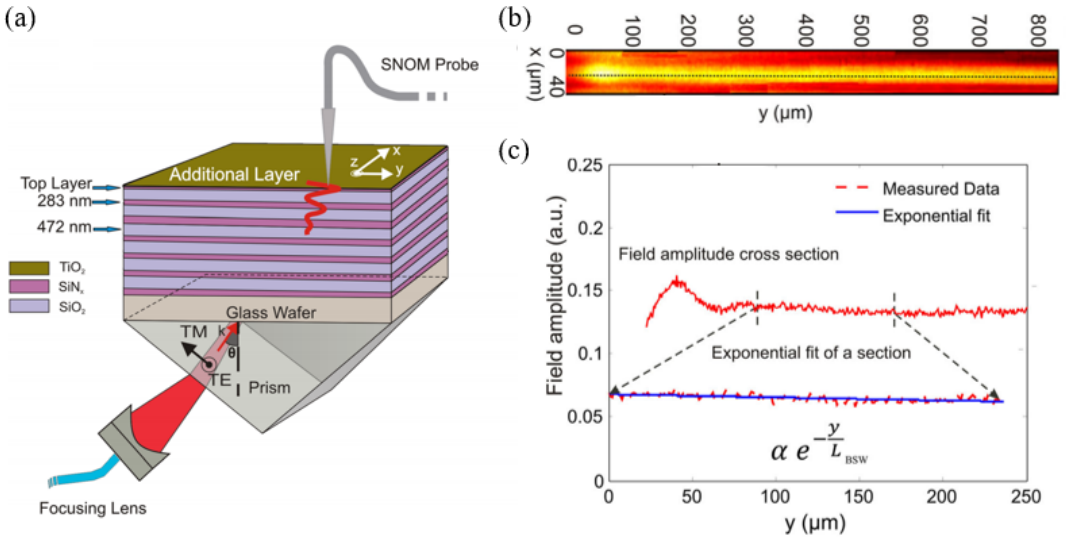

Figure 1-4 (a) Schematic of the BSW coupling on a dielectric multilayer platform. (b) Multi-heterodyne scanning near field optical microscopy image demonstrating BSW

propagation in the near-field. (c) Exponential fit of the field amplitude along the direction of propagation to measure the propagation length [18].

In recent years, BSWs have drawn a great deal of attention and have been studied extensively for various applications including sensors [20–22] and components of photonic integrated circuitry such as photodetectors [23] and waveguides [24–27], ring resonator [28], and Mach−Zehnder interferometers [29].

1.3 Surface plasmon wave versus Bloch surface wave

SPW is a type of electromagnetic surface wave that propagates at the interface between metal later and dielectric medium, the dielectric medium is usually air or water. Due to the high loss of the metal layer, the propagation length is quite short (<100μm), the operating wavelength is also very limited (mostly in the Visible region).

BSW is also a type of electromagnetic surface wave, different from SPW, BSW propagates at the interface between dielectric medium and dielectric multilayer. Due to the very low loss of dielectric material, the propagation length of BSW is much longer than that of SPW, the propagation length of BSW has been demonstrated up to mm order [18]. Additionally, because several dielectric materials have good optical properties in different wavelength ranges, the operating wavelength range of BSW is very broad. The BSW has been demonstrated in visible [30] near-infrared [20] and mid-infrared regions [31]. The summary of the comparison of surface plasmon wave and Bloch surface wave is shown in Figure 1-5.

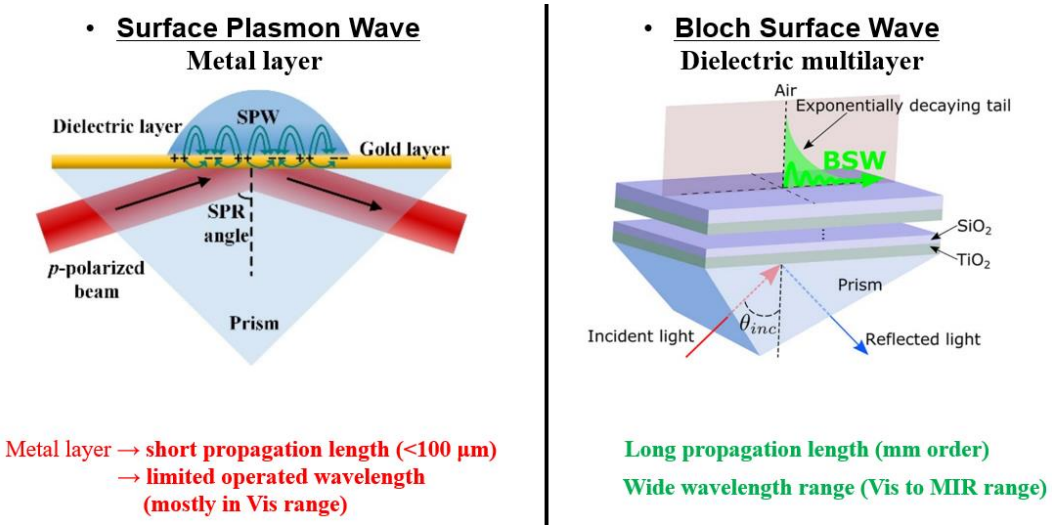

Figure 1-5 Surface plasmon wave versus Bloch surface wave

Chapter 2 : Manipulation of BSW on a chip: slab-guided BSW

2.1 Introduction

The Photonic integrated circuits (PICs) offer significant advantages over electronic circuits, such as low-loss information transport and faster information processing [32–34]. A variety of devices including modulators [35], photodetectors [36], optical multiplexers [37], and spectral filters [38] have been demonstrated on PIC platforms in the past decades. The BSW-based PIC opens new possibilities in the applications of a low-loss surface wave such as a biosensor. To realized the BSW-based PIC, the manipulation of BSW on a chip is needed. The basic and important components, coupler and waveguide, are required for the manipulation of BSW. The grating coupler for BSW coupling has been demonstrated as shown in Figure 2-1 [39]. The grating couplers perpendicular to each other are designed for different polarization directions (P1 and P2) of incident light as shown in Figure 2-1 (a), (b), and (c). The light with P1 and P2 polarized will couple into BSW and propagate to x- and y-direction, respectively. The fabricated sample is shown in Figure 2-1 (d), the ridge A and B are used for scattering light out for observing the coupled BSW in x- and y-direction, respectively. The experimental results are shown in Figure 2-1 (e) and (f). The incident light with P1 and P2 polarized are coupled into BSW and propagates to x and y direction until scattering out from ridge A and B, respectively. The light intensity distribution as shown in Figure 2-1 (g) clearly shows the incident light is coupled into BSW and scattered out from the ridge.

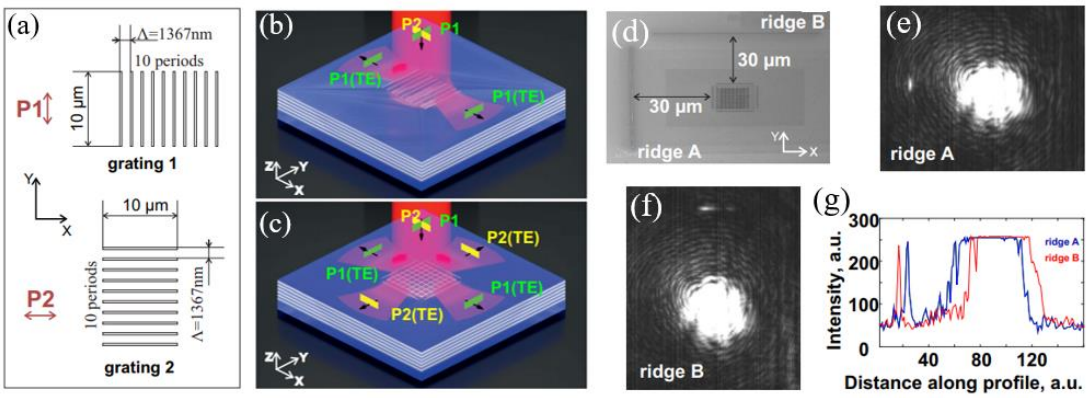

Figure 2-1 (a) Polarization with respect to gratings. (b) Illustration of the BSW coupling at the single grating (c) Illustration of the BSW coupling at the inter-crossed grating. (d) SEM image of sample (e) Camera image of the horizontally coupled BSW (f) Camera image of the vertically coupled BSW (g) Cross-sections for vertically and horizontally couple BSWs [39].

The BSW guided by polymeric ridges has also been demonstrated as shown in Figure 2-2 [24]. The schematic diagram of the realization of guided-BSW is shown in Figure 2-2(a). Light is coupled into BSW by the prism and propagates on the ridge. The scanning near field optical microscope probe is used to characterize the propagation of guided-BSW on the polymeric ridge. Figure 2-2 (b) shows the intensity distribution of the polymeric ridge on the BSW platform shows the field exponentially decay in the air and in the BSW platform, which is a typical BSW mode. The experimental results of the characterization of the propagation of guided-BSW are shown in Figure 2-2 (c) and (d). In this study. the BSW platform is designed for TM-polarized light, so the TM-polarized light will not couple into BSW as shown in Figure 2-2 (c). For the TE-polarized light, the light is couple into BSW and propagate on and polymeric ridge with good confinement as shown in Figure 2-2 (d).

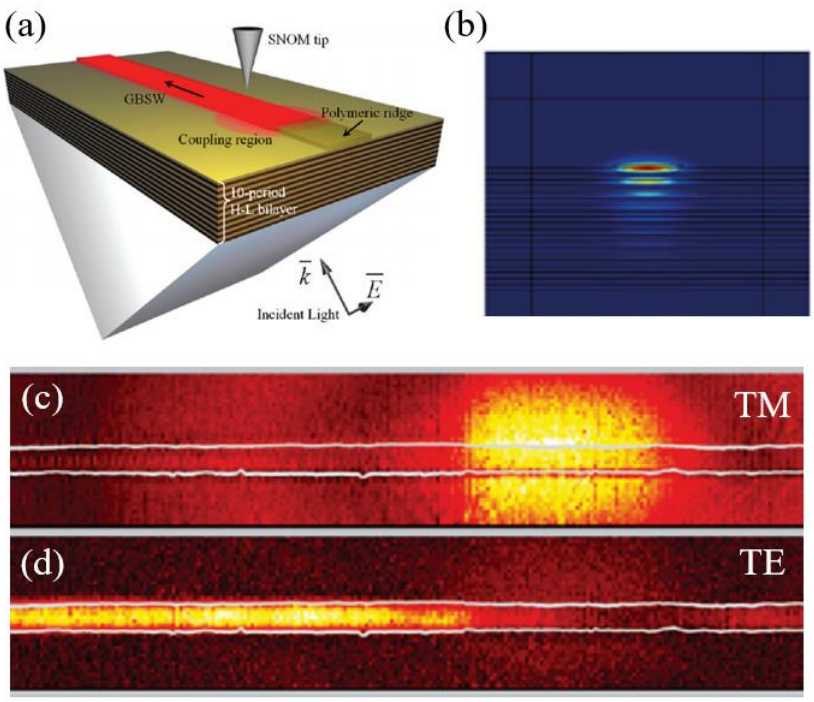

Figure 2-2 (a) Light couple into BSW and propagates on the polymeric ridge by the prism. (b) The guided-BSW total intensity distribution of polymeric ridge on BSW platform (c) Airy-like near-field amplitude distribution upon TM-polarized illumination. (d) Guided BSW field amplitude distribution on the polymeric ridge upon TE-polarized illumination [24].

However, although both BSW coupling using the line grating coupler [40] and the BSW guiding through a guiding slab [24] have been demonstrated, the integration of grating coupler and guiding slab in a single device has yet to be demonstrated. The integration of the grating coupler and guiding slab is critical in the development of the BSW-based PIC.

2.2 Light couple into BSW by grating coupler and guided by guiding slab

The schematic diagram of the grating coupler and guiding slab on the dielectric multilayer BSW platform is shown in Figure 2-3. The TE-polarized light couple into BSW by the grating coupler and propagate on guiding slab on 5-pair Si/SiO_2 dielectric

multilayer BSW platform. To achieve BSWs with low propagation losses at telecommunications wavelengths, Si and SiO_2 were selected as the high and low index materials, respectively, due to their low absorption coefficients over the telecommunications wavelength range.

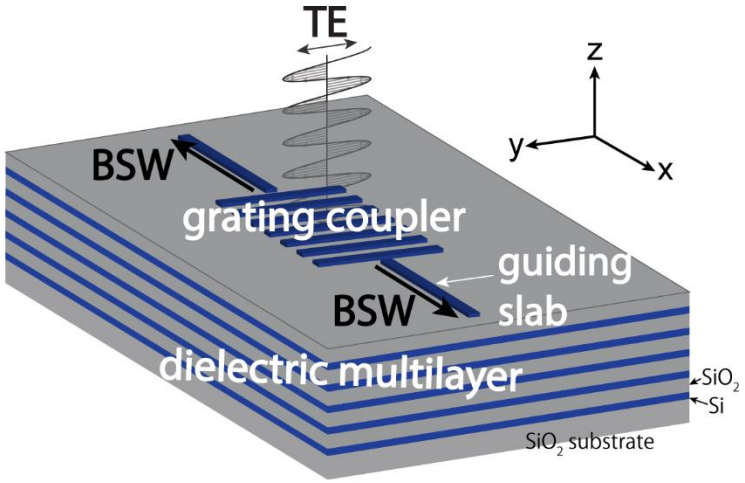

Figure 2-3 Schematic diagram of grating coupler and guiding slab on Si/SiO_2 BSW multilayer

Under normal incidence, the grating period Λ can be estimated from the target wavelength λ by

$$\Lambda = \frac{\lambda}{n_{\text{eff}}}$$

where n_{eff} is the effective mode index of the BSW mode. The Beam Propagation Method (BPM) (BeamPROP, RSoft Design Group, Ossining, U.S.A.) was used to find a guided mode as shown in Figure 2-4 (a). The layer thicknesses were optimized to be 190, 378, and 40 nm for the Si layer, SiO2 layer, and Si top layer, respectively. For a guiding slab with a width of w = 700 nm and height of h = 40 nm, the effective mode index of the resulting BSW mode is n_{eff} = 1.24 and the effective wavelength is $\lambda_{BSW} = \frac{\lambda}{n_{\text{eff}}}$ =1250 nm. Starting from the initial calculated value, the grating period Λ is then optimized using a

finite-difference time-domain (FDTD) simulation (FullWAVE, Rsoft Design Group, Ossining, U.S.A.) in which a Gaussian beam (λ = 1550 nm, TE-polarized normal incident) is shone onto the grating coupler and examining the efficiency of BSW excitation. The grating period Λ and the slab width s were varied to obtain maximum BSW coupling efficiency by finding the conditions for maximum absorption. The schematic of the behavior of light in the grating coupler and dielectric multilayer BSW platform is shown in Figure 2-4(b). To optimize the grating coupler on the dielectric multilayer BSW platform, the absorption and transmission spectral have been simulated as shown in Figure 2-4(c). The normalized electric field E_y distribution for the optimized dimensions (period Λ = 1223 nm and slab width s = 832 nm) of the grating coupler and dielectric multilayer BSW platform is shown in Figure 2-4(d). The amplitude of the electric field was found to be at the maximum at the top layer and negligible in the vicinity of the substrate. These two observations together indicate that the TE-polarized incident light is well coupled into the BSW, and the maximum coupling is reached by the designed grating coupler.

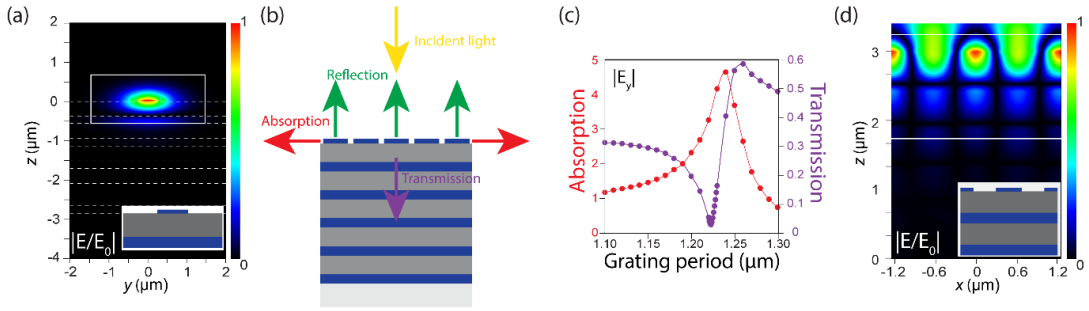

Figure 2-4 Characterization of the grating coupler and the guiding slabs on the dielectric multilayer BSW platform. (a) Normalized electric field E_y amplitude distribution (y–z plane) of the BSW that propagates along with the guiding slab. (b) Schematic of the behavior of light in the grating coupler and dielectric multilayer BSW platform. (c) The absorption and transmission of the grating coupler and dielectric multilayer BSW

platform as a function of the grating period. (d) Normalized electric field E_y amplitude distribution (x−z plane) of the grating coupler. (e) Normalized electric field energy density $E_{density}$ distribution along an x−y plane through the center of the top Si layer when the grating coupler is illuminated by TE-polarized light. BSW propagates along with the guiding slabs on the left and right sides of the grating coupler. The insets of (a) through (c) show schematics of the cross-sections used in each respective figure.

The coupling of normal TE-incident light to a guided BSW using a grating coupler connected to a guiding slab on a dielectric multilayer BSW platform is further confirmed using 3D FDTD simulations. Figure 2-5 shows the normalized electric field energy density ($E_{density}$) distribution in the x−y plane for the grating coupler under illumination by TE-polarized light (λ = 1550 nm, Gaussian beam). The guiding slab ensures the coupled light is confined and propagates along with the guiding slab. The theoretical propagation loss of the guided BSW is zero under the assumption of a semi-infinite one-dimensional photonic crystal (dielectric multilayer), real devices have a finite number of periodic layers, and this introduces a finite propagation loss caused by light leaking out through the substrate. In contrast to surface plasmon polaritons, which have inherent metal losses, the BSW propagation losses can be reduced by increasing the number of layer pairs and also employing high-quality deposition techniques (e.g., plasma-enhanced chemical vapor deposition) [19] that can realize extremely low loss dielectric materials.

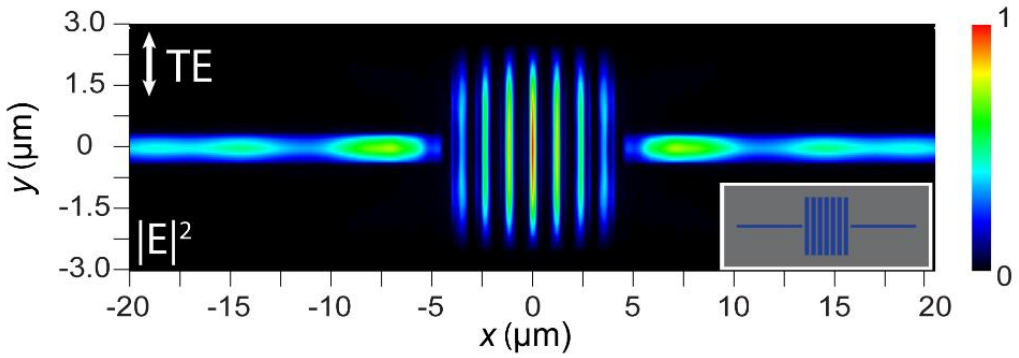

Figure 2-5 Characterization of the grating coupler and the guiding slabs on the dielectric multilayer BSW platform. Normalized electric field energy density $E_{density}$ distribution along an x−y plane through the center of the top Si layer when the grating coupler is illuminated by TE-polarized light. BSW propagates along with the guiding slabs on the left and right sides of the grating coupler. The inset show schematics of the cross-sections used in each respective figure.

Following the design and optimization of the grating coupler and guiding slab on the dielectric multilayer, the device has been fabricated. The thicknesses of 5-pair Si/SiO_2 multilayer BSW platform, Si and SiO_2, with thicknesses of 190 and 378 nm, respectively, were deposited on a SiO_2 substrate using an RF-magnetron sputtering system (CFS-4ES, Shibaura Engineering Works Co., Ltd., Yokohama, Japan). Guiding slab and grating coupler patterns were defined by electron beam (EB) lithography. The electron beam resist (ZEP520A, Zeon Corporation, Tokyo, Japan) was spin-coated at 3000 rpm with a thickness of about 400 nm. The exposure dose of the electron beam system (F7000SVD02, Advantest, Tokyo, Japan) was set to 104 μC/cm2. The development was performed using n-amyl acetate as a developer and methyl isobutyl ketone and isopropyl alcohol for rinsing. The Si top layer with a thickness of 40 nm was deposited on top of the patterned resist. The lift-off process removed the resist with Si top layer. Dimethylacetamide was used as a stripper in the lift-off process. The process

was done at room temperature. The SEM image of the fabricated 5-pair Si/SiO_2 multilayer, grating coupler, and guiding slab is shown in Figure 2-6.

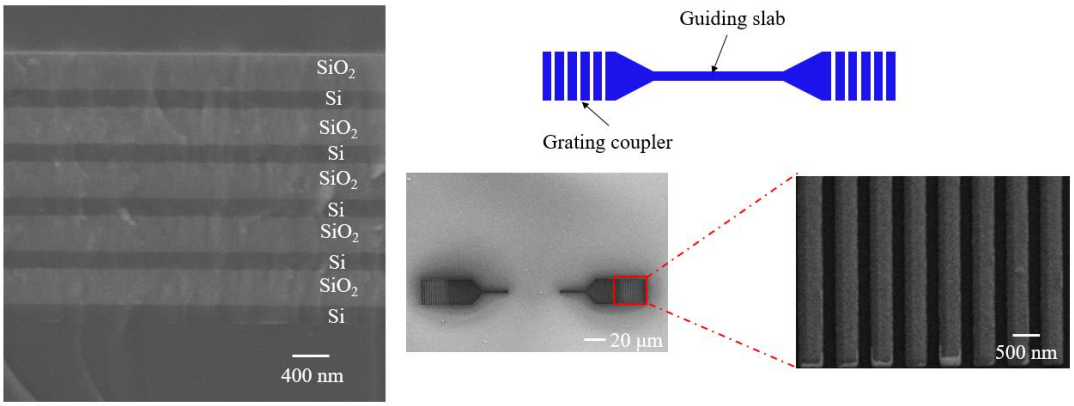

Figure 2-6 SEM image of the 5-pair Si/SiO_2 multilayer, grating coupler, and guiding slab

2.3 Propagation length of slab-guided BSW

The experimental setup used to investigate the incident light coupled to BSW and the propagation length of BSW is shown in Figure 2-7. The tunable laser with C-band and L-band wavelength range as the light source. The collimator is used to have the laser beam from fiber become a plane wave beam. The polarization of the laser light is controlled by a polarizer. The NIR camera is used to capture reflected light from the sample and will also detect light out-coupled from the grating coupler.

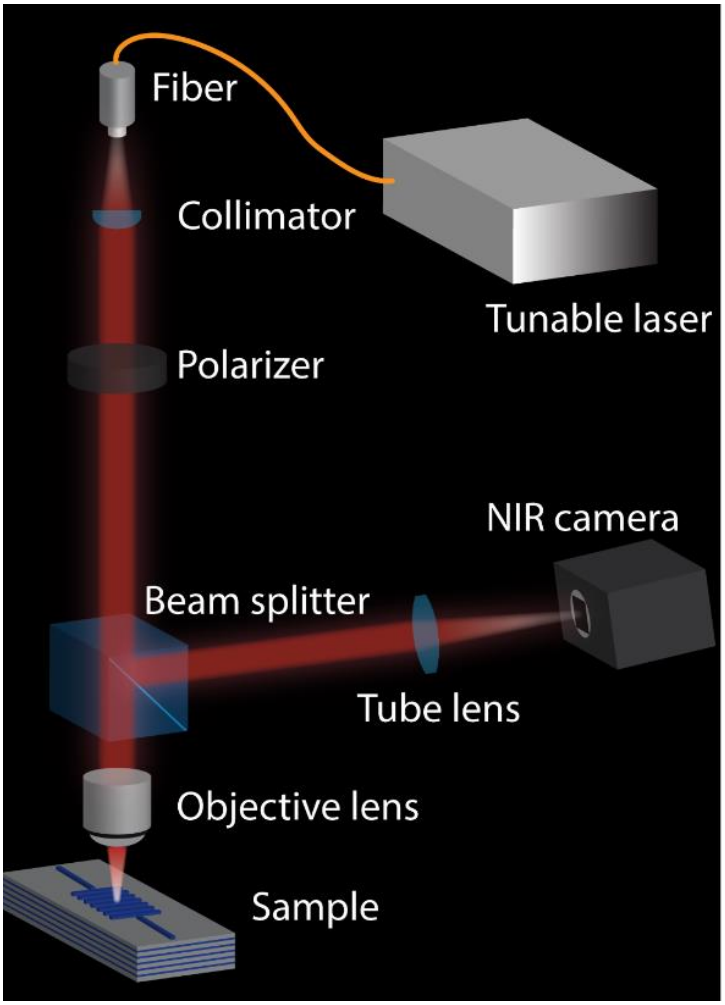

Figure 2-7 Experimental setup used to couple incident light to a guided BSW and collect the out-coupled light.

Figure 2-8 shows the NIR images captured by NIR camera with the experimental setup shows in Figure 2.4. The fabricated grating couplers connected with the guiding slab on the dielectric multilayer BSW platform can be seen in the NIR image as shown in Figure 2.5(a). When the left grating coupler under normal TE-polarized illumination, the light coupled into BSW in the guiding coupler and propagated to the right side, and then out coupled from the grating coupler on the right side as shown in Figure 2-8 (b).

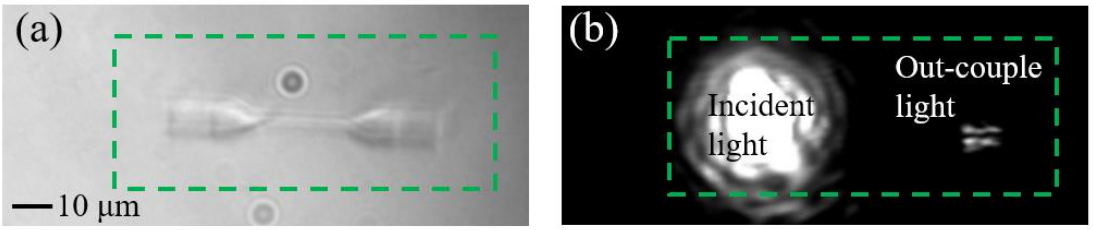

Figure 2-8 (a) NIR images of 20 μm-long guiding slab (b) NIR images of 20 μm-long guiding slab under TE-polarized illumination. Reflected light from the in-coupling grating is observed on the left, and decoupled light from the out-coupling grating is observed on the right

To study the propagation length of BSW, the devices with different lengths of guiding slabs have been fabricated. Figure 2-9 (a) shows NIR images of different length guiding slabs with grating couplers on either end. Light is incident on the grating couplers on the left and is coupled into a guided BSW that propagates along with the guiding slabs to the grating couplers on the right side where the out-coupled light can be seen as a bright spot. The light intensity of the bright spot on the right side then is analyzed by using image processing software ImageJ. The integrated intensity of the out-coupled light for different guiding slab lengths is shown in Figure 2-9 (b). The result is fit to an exponential decay which gives an estimated propagation length of 135 μm for the guided BSW mode. In comparison to the very short propagation lengths of the SPPs (≈ 10 μm) reported in the literature the observed BSW, propagation length is one order longer [41–44], the based on lab-guided BSW will be introduced in the ex section.

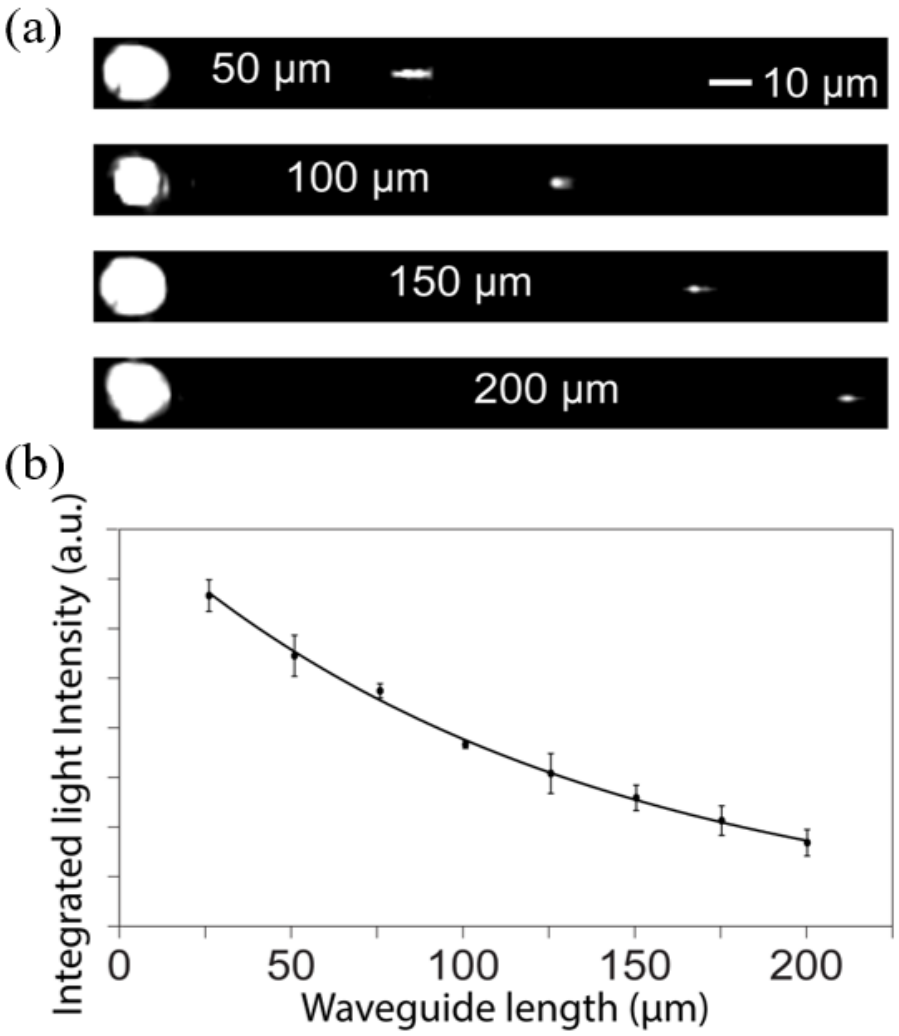

Figure 2-9 Coupling and propagation of a guided BSW on a dielectric multilayer BSW platform. (a) NIR images of 50, 100, 150, and 200 μm-long guiding slabs under TE-polarized illumination. Reflected light from the in-coupling grating is observed on the left, and decoupled light from the out-coupling grating is observed on the right. (b) The integrated intensity of the out-coupled light spot from guiding slabs of varying lengths is plotted against their length. The result is fitted to an exponential decay curve.

Coupling and propagation of a guided BSW on a dielectric multilayer BSW platform. (a) NIR images of 50, 100, 150, and 200 μm-long guiding slabs under TE-polarized illumination. Reflected light from the in-coupling grating is observed on the left, and

decoupled light from the out-coupling grating is observed on the right. (b) The integrated intensity of the out-coupled light spot from guiding slabs of varying lengths is plotted against their length. The result is fitted to an exponential decay curve.

Chapter 3 : Slab-guided BSW based logic gate

3.1 Introduction

The all-optical logic gate devices have attracted enormous attention because of their critical applications in the fields of information processes and the development of photonic integrated circuits [45–47]. There are various approaches to realize the all-optical logic gates such as semiconductor optical amplifier [48] and the formation of constructive/destructive interference in the photonic-crystal structure [49]. The working principle of the photonic crystal interference-based all-optical logic gate is shown in Figure 3.1. 2D photonic crystal consist of parallel rods embedded on a substrate. Since light cannot propagate in the photonic crystal at the designed wavelength, if the defect is introduced into the 2D photonic crystal, the line defect would work as a waveguide. The defect line as input and output waveguide is shown in Figure 3-1(a). The four images on the top of Figure 3.1(b) show the NOR gate. The input middle waveguide is set to be always in the on-state. Thus when neither input A nor input B is in the off-state, the output will be in the on-state. When either input A or input B is in the on-state, due to the destructive interference between input A and input middle or input B and input middle, the output will be in the off-state. Finally, when both input A and input B are in on-state, the destructive interference is also formed result in the off-state in the output. The four images on the bottom of the Figure 3-1(b) show the AND gate. In the case of AND gate, the input middle is set to be off all the time. Therefore, when both input A and input B are in the off-state, the output is in the off-state. When either input A or input B is in the on-state, the output will be in off-stated due to the power from

only one input is too low. When both input A and input B are in the on-state, the output will be on due to the constructive interference formation from two inputs.

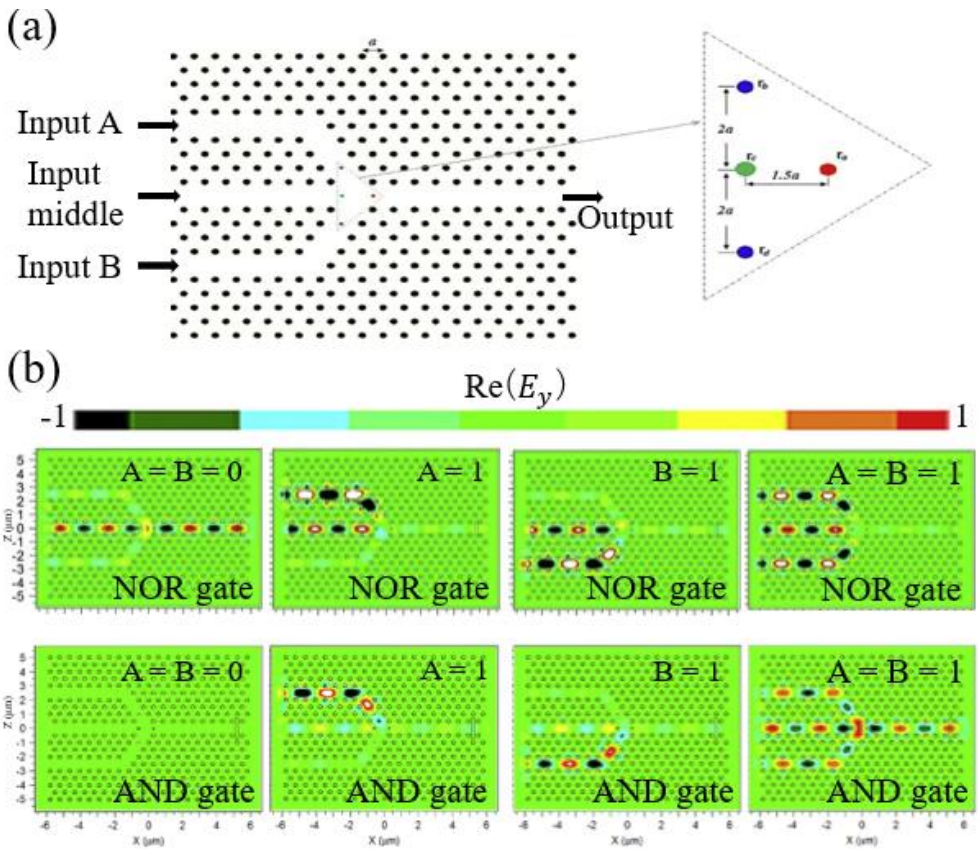

Figure 3-1 (a) Schematic diagram of the NOR and AND gates based on photonic crystal (b) Electric filed propagation for NOR gate and AND gate [50].

Although several types of logic gates are realized based on the photonic-crystal structure platform, the intrinsic instability and low extinction ratio between on and off-state hamper it to be used to build a practical photonic circuit [51]. To overcome this issue, the all-optical logic gates that utilize the linear interference between surface plasmons polariton (SPP) modes has been demonstrated [52,53] with a fairly high extinction ratio

(~20 dB) between on- and off-state which is higher than that of the optical amplifier [54] (~8.5 dB) and photonic-crystal structure [51] (~16 dB) based logic gate.

The working principle of the all-optical logic gate based on the linear interference of SPP mode is shown in Figure 3-2. The plasmonic slot waveguides, consisting of air slots etched in a thin gold film as shown in Figure 3-2(a). These structures can provide SPP modes that are strongly confined at the interface of the dielectric waveguide and metal film. The logic operation of the XOR gate is shown in Figure 3-2(b). The grating coupler on the left side is used to couple incident light into SPP mode, and the grating coupler on the right side is used to couple light out to check the state of the output. The XOR gate has an asymmetric Y-shape configuration, which can cause the formation of destructive interference between two SPP modes. For the logic operation, when either input A or input B is in the on-state, the output will also be in the on-state. When both input A and input B are in the on-state, the output will be off-state due to the formation the destructive interference between two SPP modes. The extinction ratio, which is the power ratio between on- and off-state, is up to 24 dB in this SPP-based logic gate. The SPP all-optical logic gate path the way for developing dense on-chip photonic/plasmonic integrated circuit.

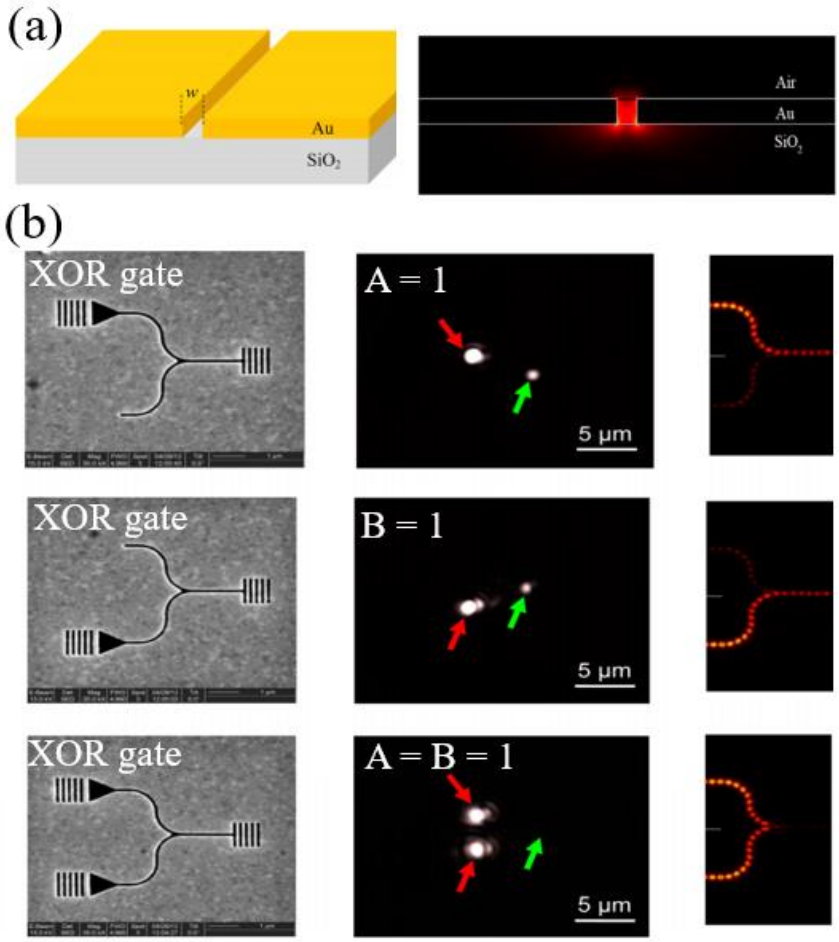

Figure 3-2 (a) Schematic diagram of the plasmonic slot waveguide structure and the power density profile of a 530 nm SPP mode. (b) Logic operation of the SPP-based XOR logic gate [52].

However, despite the well-investigated SPP-based device, the intrinsic ohmic losses from electronic excitation in their metal layers have been seen as a bottleneck for building a practical photonic/plasmonic integrated circuit with low propagation loss.

To overcome the issue of the low extinction ratio of the photonic crystal-based logic gate and the high loss of the SPP-based logic gate, the BSW-based logic gate is proposed in this thesis. BSW-based devices can overcome the issues of SPP-based devices such as limited operated wavelength and low propagation length. The proposed BSW-based logic gate is based on the interference of BSWs by the broadside radiation from the

near-zero-index waveguides. Near-zero-index material and near-zero-index waveguide will be introduced in the following section.

The definition of the refractive index n is:

$$n = \sqrt{\mu\varepsilon}$$

where the μ is permeability and ε is permittivity. The definition of the refractive index shows that the index is determined by its response to both electric and magnetic fields of light. The propagation of light within a material can be dictated by the refractive index. The effective wavelength which is defined by the rate of phase accumulation is also related to the refractive index. The schematic diagram that considering light entering material with different values of refractive index is shown in Figure 3-3 [55]. When light entering the material with a refractive index higher than one, then the light will propagate with a shorten wavelength compare to that of the light in free space. On the other hand, when light entering the material with a refractive index smaller than one, then the light will propagate with s longer wavelength compare to that of the light in free space. For the special case, the light entering the material with zero indexes, the light will propagate with an infinity wavelength as shown in Figure 3-3.

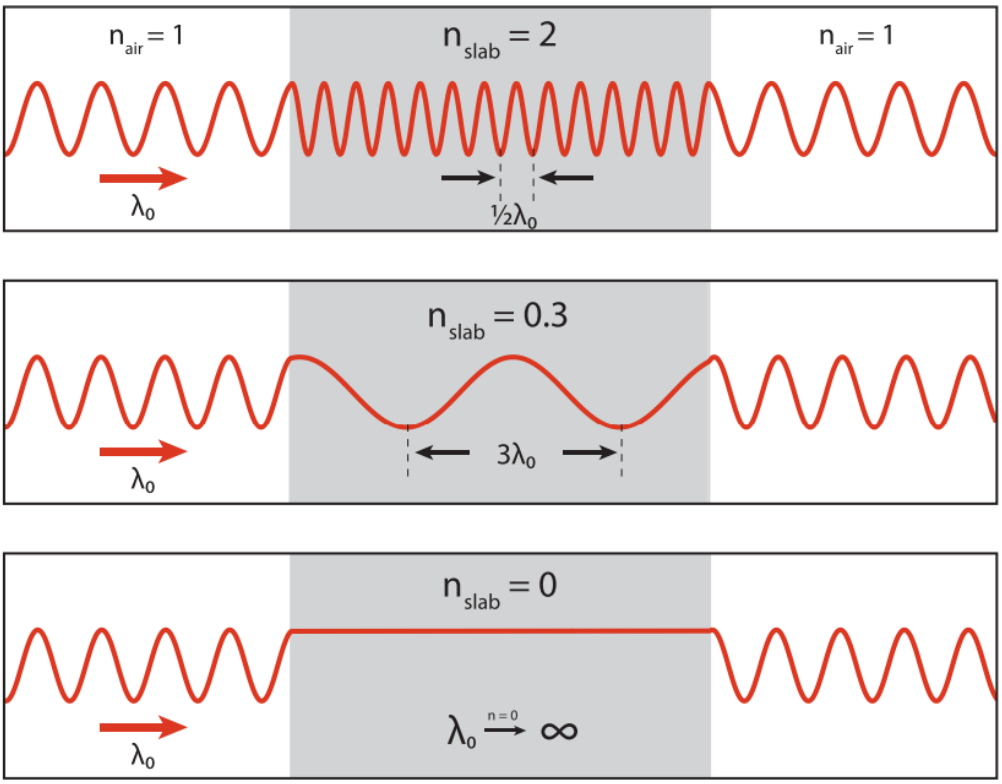

Figure 3-3 The wavelength of light propagating through dielectric media is changed in inverse proportion to the refractive index. The wavelength extends to infinity as the real portion of the refractive index decrease to zero [55].

To achieve zero-index, one or both of the two parameters must be zero. When the refractive index equal to zero, some uncommon phenomena will occur that can be predicted from the wave equation:

$$\nabla^2 E - \frac{\mu\varepsilon}{c^2}\frac{\partial^2 E}{\partial t^2} = 0$$

where E is the electric field, c is light speed and t is time. When the refractive index of a material is equal to zero results in the $\nabla^2 E = 0$ which indicates the electric field oscillates in time, rather than in space. The field distribution will be uniform in the entire material that shows phase-free and infinite effective wavelength as shown at the bottom of Figure 3-3. There is another phenomenon of the zero-index material called broadside

radiation. Considering a light source in the zero-index material and the material is surrounded by air as shown in Figure 3-4. The light is emitted by the light source and goes outward to the air. According to Snell's law, the incident angle θ and the refraction angle α can be expressed as:

$$n \sin \theta = n_{air} \sin \alpha$$

For a zero-index material, the refraction angle is always zero due to the n is equal to zero. The light will radiate away from the material normal to its surface, which forms the broadside radiation as indicated in Figure 3-4.

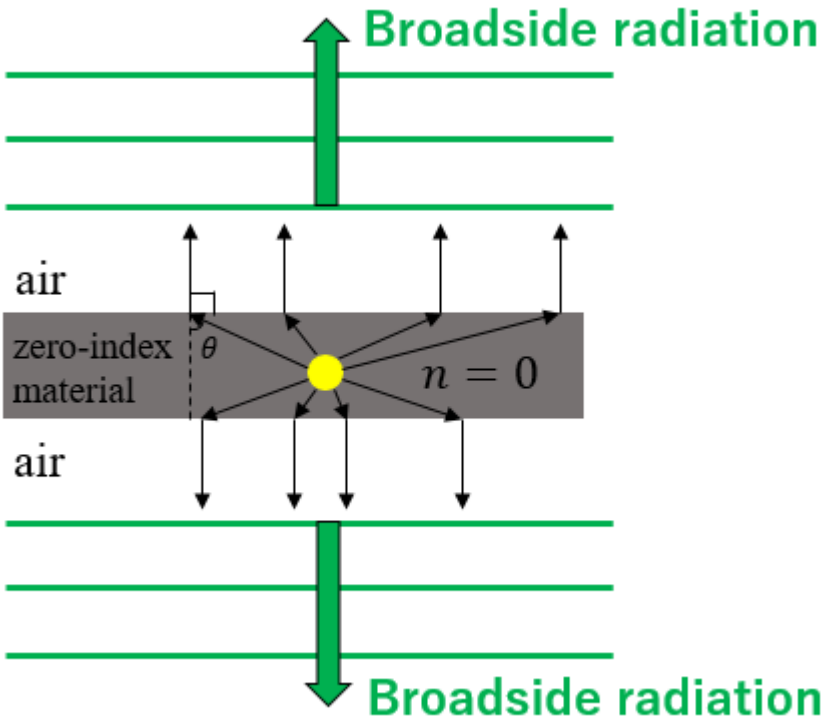

Figure 3-4 Broadside radiation from zero-index material.

Zero-index material shows interesting phenomena such as phase-free propagation, infinite effective wavelength, and broadside radiation from its surface. One approach to access zero-index properties is directly using the material with a refractive index near

zero. Epsilon-near-zero material such as Al-doped zinc oxide and indium tin oxide which possessed near-zero-index properties have been widely studied for optoelectronic devices [56–58]. However practical implementation of on-chip integration application requires compatibility with complementary metallic-oxide-semiconductor technologies. The zero-index metamaterial consisting of a square array of air holes in a 220-nm-thick silicon-on-insulator wafer has been demonstrated as shown in Figure 3-5 [59]. The schematic design of the air-hole array structure zero-index with air hole radius r and period an as resonator is shown in Figure 3-5(a). Figure 3-5(b) shows the magnetic field distribution over a unit-cell cross-section in the plane of the array, either the dipole mode or the quadrupole mode would exist which depends on the frequency of entering light. The three-dimensional dispersion surfaces that indicate the frequency dependence of these of the dipole mode and the quadrupole mode are shown in Figure 3-5(c). As the wave equation mentioned before, when the refractive index of a material is equal to zero results in the $\nabla^2 E = 0$ which indicates the electric field oscillates in time, rather than in space. The two dispersion surfaces intersect at the point where the wavenumber k both in the x and y direction, which indicates the field would not oscillates in space at this frequency. The zero-index frequency of light is designed to be 193.4 THz which is the telecommunication frequency in this study as shown in Figure 3-5(c).

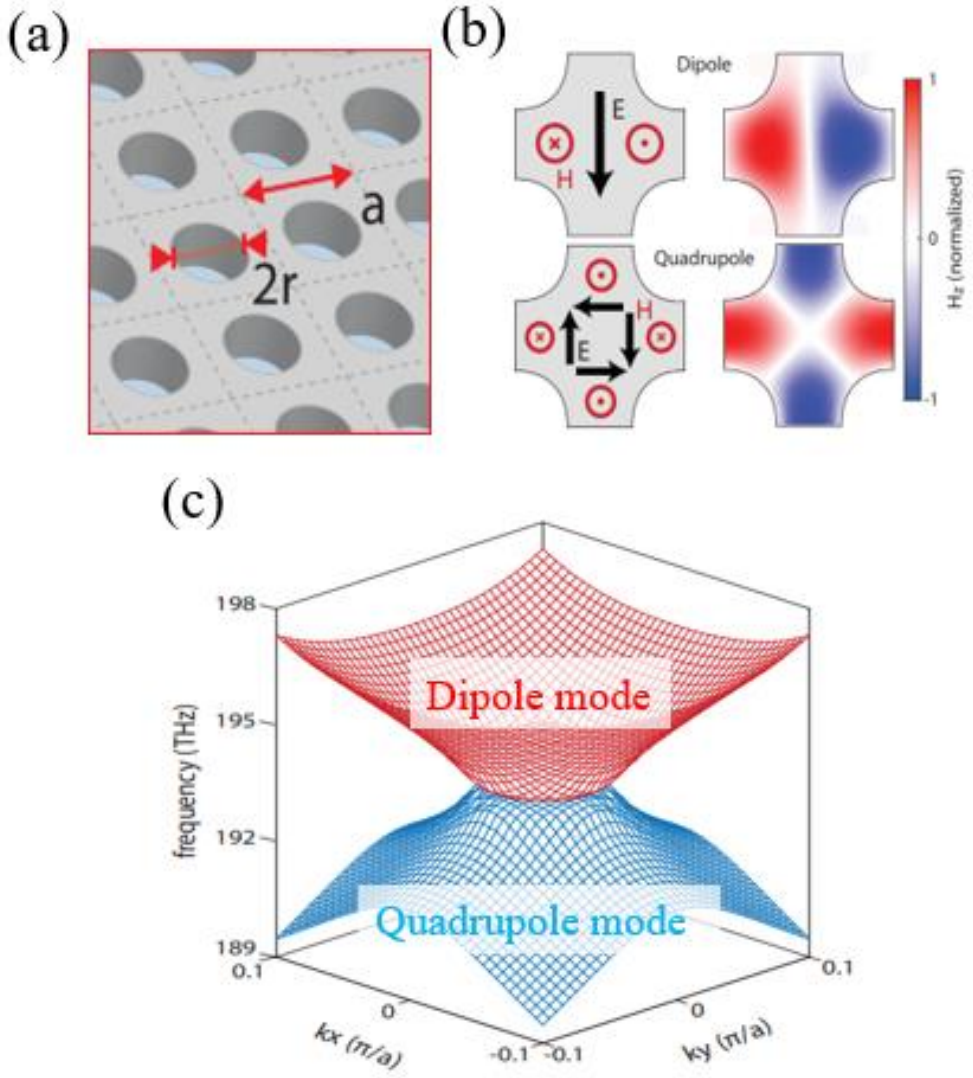

Figure 3-5 Schematic diagram of the metamaterial air-hole array with design parameters radius r and pitch a. (b) Magnetic fields over a unit-cell cross-section in the plane of the array, corresponding to an electric dipole mode and a magnetic quadrupole mode (c) Three-dimensional dispersion surfaces [59].

To characterize the air-hole array structure zero-index material, the device consists of a silicon waveguide, polymer waveguide, polymer slab waveguide, and air-hole array structure zero-index material is shown in Figure 3-6(a). The silicon waveguide is used to guide the incident light towards the zero-index material, where the light is refracted into the slab waveguide. The polymer waveguide at the outside edge of the slab

waveguide is used to scatter the output light for imaging. Figure 3-6(b) shows the SEM image of the air-hole array structure zero-index material and the testing approach. The incident light is set to be with an incident angle of 45°, the light will then leave from the air-hole array structure zero-index material with a refraction angle α, which depends on the refractive index of the air-hole array structure. Therefore, the refractive index can be obtained by observing the refraction angle α. The experimental results of the incident light at wavelength 1625 nm as shown in the near-infrared microscope image in Figure 3-6(c). The scattering light at the position of refraction angle 0° is shown in the image, which indicates the air-hole array structure would work as the zero-index material when the incident light at wavelength 1625nm. Figure 3-6(d) shows both the simulated and experiment results of the wavelength-dependent effective refractive index of the air-hole array structure. The relationship between effective refractive index and wavelength is linear along with the entire wavelength range from 1480 nm to1680 nm and in the vicinity of the zero-index wavelength of 1625 nm.

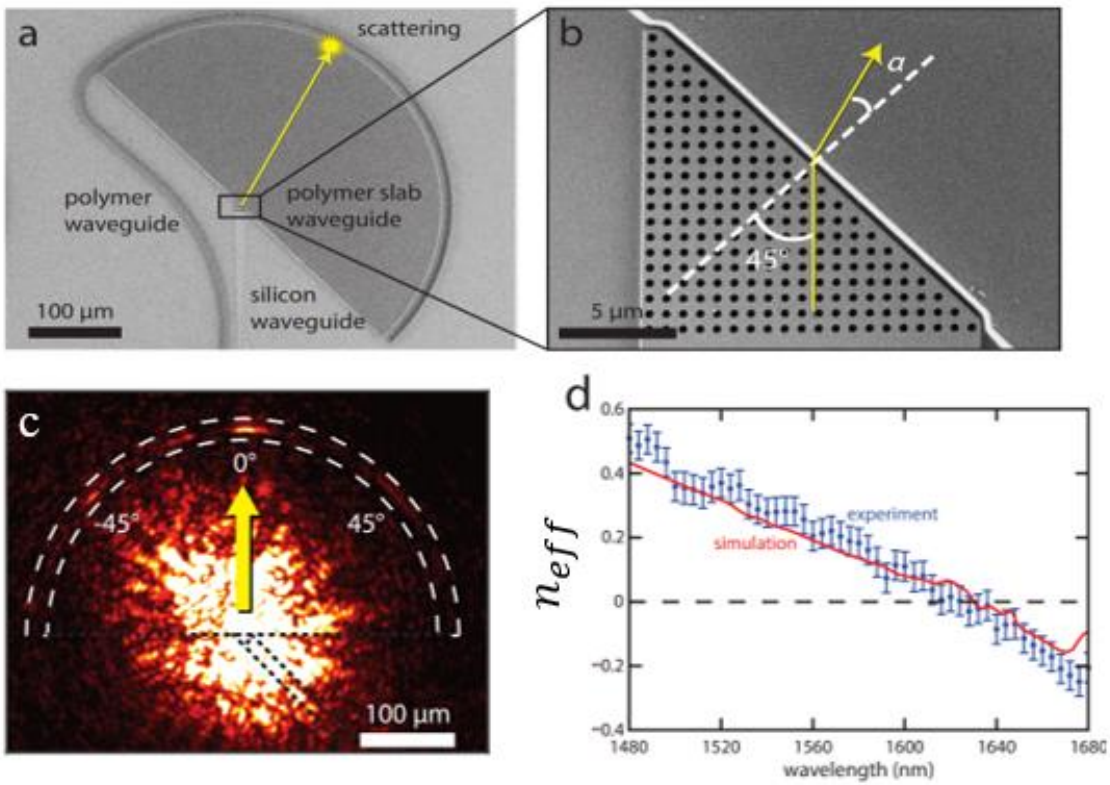

Figure 3-6 (a) SEM image of the fabricated device. A silicon waveguide carries the incident beam towards the zero-index metamaterial prism as outlined in black, where the beam is refracted into the slab waveguide. A silicon lip at the outside edge of the slab waveguide is used to scatter the output beam for optimal imaging. The angle of refraction α is determined by measuring the position of the refracted beam at the curved output edge of the polymer slab waveguide as indicated by the yellow scattering point. An additional polymer waveguide around the outside edge of the slab waveguide includes defects that are used to align the infrared images during experimental data processing. (b) Fabricated zero-index metamaterial prism showing the incident and refracted beams. (c) Near-infrared microscope image of the prism at 1625 nm, showing the refracted beam, which propagates normal to the interface between the prism and the slab waveguide. The black dotted lines indicate the position of the prism and input waveguide. The white dashed lines delineate the portion of the image that is used to

produce the measured near-field pattern. (d) The effective index of the metamaterial is extracted from the measured (blue dots) and simulated (red line) refraction angle, α. [59].

While the zero-index properties have been demonstrated with the air-hole array structure, this bulky structure is difficult to be used in the integration of the on-chip photonic application. To overcome this issue, the more convenient zero-index material structure, a corrugated waveguide has been proposed [60]. The design approach and characterization method are shown in Figure 3-7. The design principle of corrugated waveguide zero-index material is similar to that of the air-hole array structure. The corrugated waveguide is a part of the air-hole array structure as shown in Figure 3-7(a). Figure 3-7(b) shows the dispersion curve of the two modes that exist in the corrugated waveguide. The two modes intersect at the point where the wavenumber β equal to zero, which indicates the field would not oscillate in space at this wavelength. The field distribution over a unit-cell of the corrugated waveguide when operated at the zero-index wavelength is shown in Figure 3-7(c). The hybrid mode when operated at the zero-index wavelength contains both an electric dipole and a magnetic dipole resonance in quadrature.

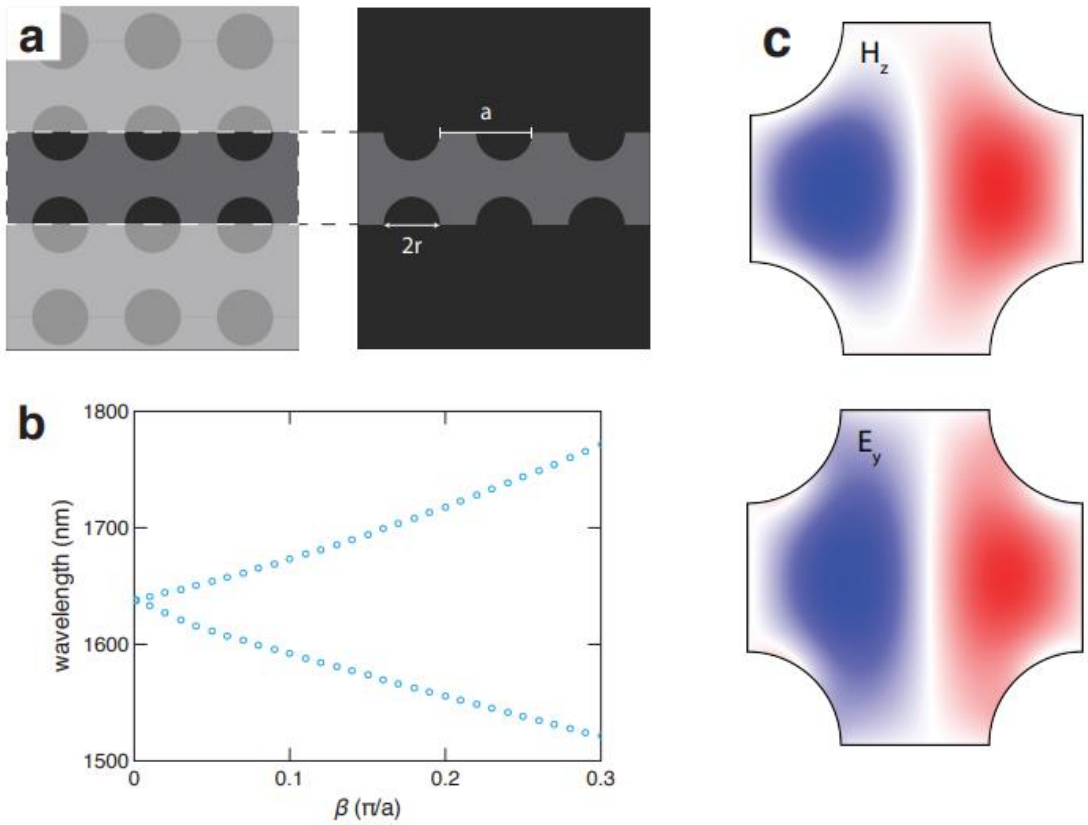

Figure 3-7 (a) Schematic of zero-index waveguide consisting of a single-channel zero-index material. (b) The band structure for this waveguide possesses a pair of modes that intersect at β = 0. (c) The magnetic H-field perpendicular to the plane of the device (Hz) and the out-of-phase in-plane E-field (Ey) for the mode when operated at the zero-index wavelength [60].

To characterize the corrugated waveguide, the standing wave was formed in the corrugated waveguide by having two lights entering from both sides coherently as shown in Figure -.8(a). The resulting standing wave shows regularly spaced nodes separated by a distance corresponding to $\Delta z = (\lambda_0/2n_{eff})$, thus, the effective refractive index n_{eff} can be obtained by analyzing the distance between two nodes of a standing wave Δz. Figure 3.8(b) shows the microscope images of the corrugated waveguide when two light entering from both sides coherently with a wavelength range from 1575 nm to 1675 nm. As we can observe from the figure, the light intensity is roughly the same over

the whole corrugated waveguide appears no nodes at wavelength 1625 nm which is found to be the zero-index wavelength. When the operated wavelength of the incident light away from the zero-index wavelength, the nodes started to occur in the corrugated waveguide. The distance between two nodes Δz is decreased with the more difference between the operating wavelength and the zero-index wavelength can be seen in Figure 3-8(b). The effective refractive index n_{eff} estimated by observing standing wave patterns is shown in Figure 3-8(c). The values of n_{eff} show linear dispersion through zero indexes, crossing zero at the operating wavelength at 1625 nm.

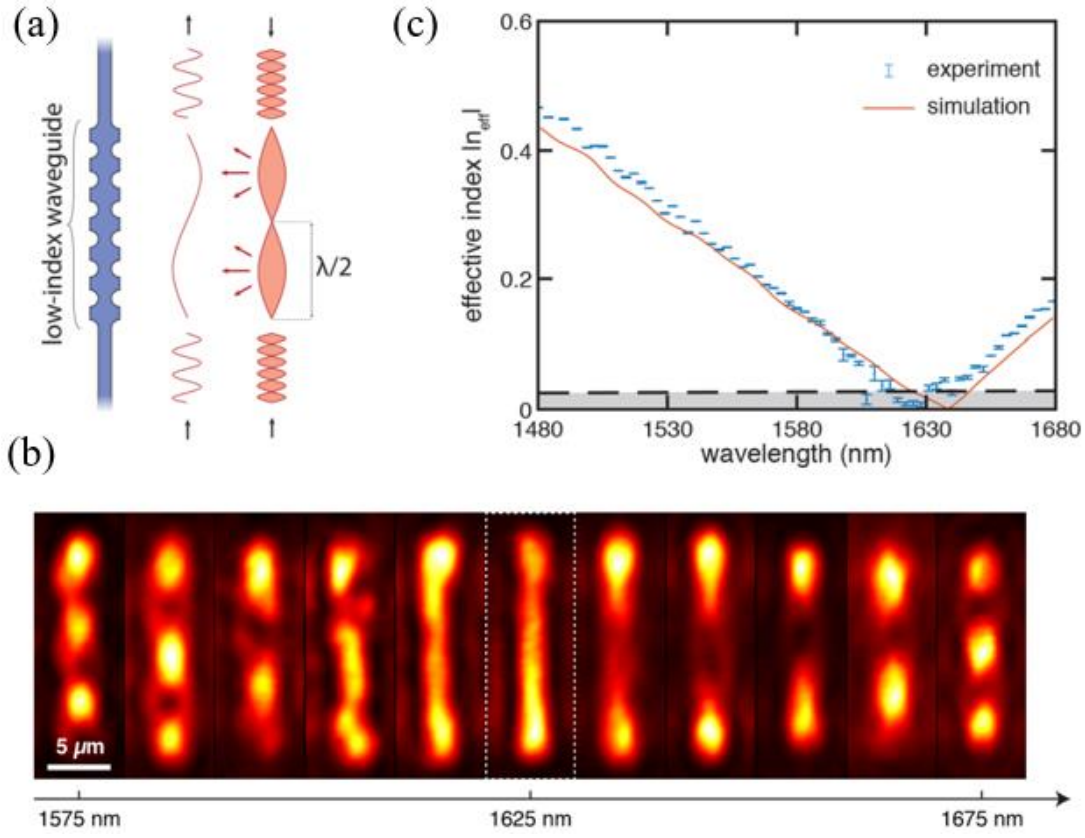

Figure 3-8 (a) A standing wave is formed when light enters coherently from both sides, which can be imaged directly in a low-index waveguide. The distance between the nodes in the standing wave is proportional to the effective wavelength. (b) Distance between the nodes increases as the operating wavelength approaches the zero-index wavelength (λ = 1627 nm). (c) The absolute value of the effective refractive index of a

zero-index waveguide attains a value near zero at $\lambda = 1627$ nm, in good agreement with simulated extracted indices. The black dashed line indicates the minimum effective index that can be measured using a 15-μm-long waveguide [60].

The zero-index properties such as phase-free and infinite effective wavelength have been demonstrated with the corrugated waveguide as mentioned in the previous study. The other zero-index property, broadside radiation, was demonstrated in the other study with the same structure as shown in Figure 3-9 [61]. The broadside radiation is demonstrated by waveguide-to-waveguide coupling. Figure 3-9(a) and (c) show the traditional waveguide-to-waveguide coupling realized by the evanescent coupling between two silicon waveguides. The evanescent field from the input waveguide is difficult to couple to the second waveguide when the gap is too large as shown in Figure 3-9(c). Comparing to the traditional waveguide-to-waveguide coupling, the waveguide-to-waveguide coupling by using a zero-index waveguide can be realized with a much larger gap due to the high intensity of broadside radiation as shown in Figure 3-9 (b). The transmission in the output waveguide is much higher than that of the traditional waveguide.

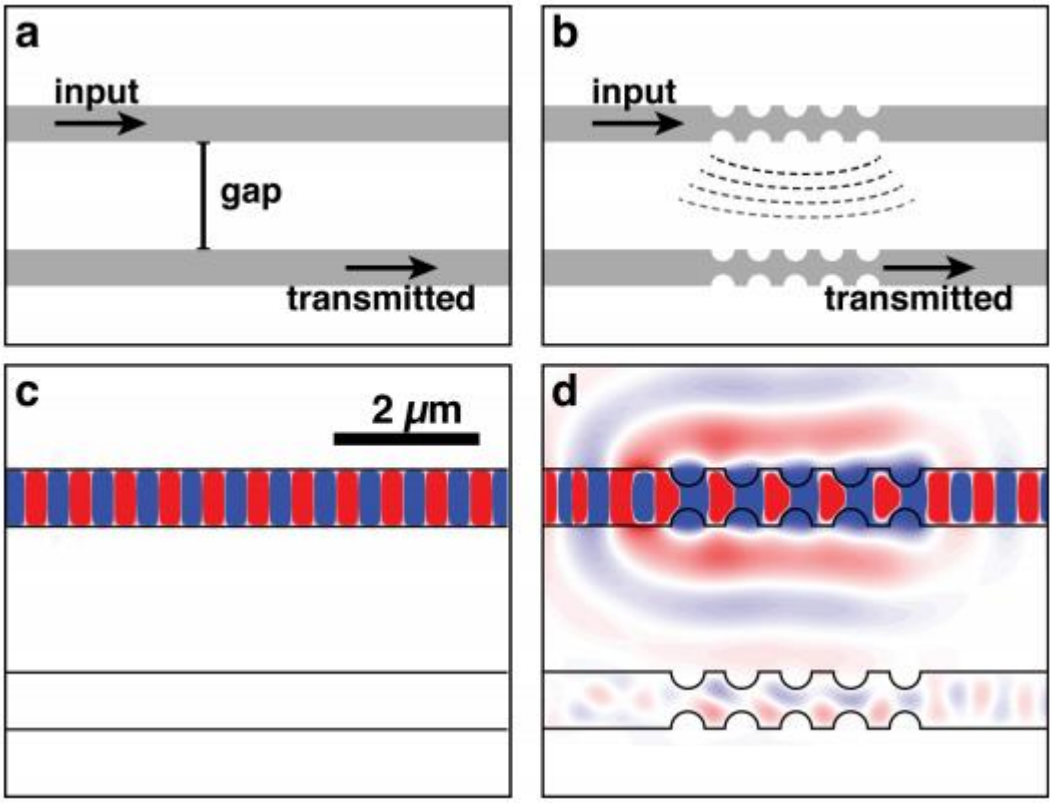

Figure 3-9 (a) In a traditional directional coupler, light propagating in one waveguide cannot transfer to the other if the gap separation is too large for evanescent coupling. b) By contrast, the zero-index waveguide-based directional coupler radiates light from one waveguide to another over the same gap. Coupling is shown by the out-of-plane component of the magnetic field Hz computed using 3D FDTD for c) the standard directional coupler and d) the zero-index coupler, both with a gap of 2 μm [61].

The design of nanostructured waveguides provides wide flexibility for PIC. These properties open up new possibilities for diverse applications such as super coupling [62] and leaky-wave far-field directive radiation [63]. The broadside radiation from the near-zero-index waveguide has the potential to be used to form constructive/destructive interference at the arbitrary position between two waveguides by carefully arranging the distance between them. The ability to form interference of the near-zero-index

waveguides enables the realization of an interference-based all-optical gate. However, the propagate distance of broadside radiation from near-zero-index waveguide on the surface is still too short to form electric/magnetic field constructive/destructive interference on the surface. Therefore, the surface wave sustainable platform is needed for building this type of all-optical logic gate. The BSW platform is an ideal candidate that can sustain the long propagation surface wave. The realization of the BSW waveguide [24,25,64] facilitates the development of BSW-based all-optical logic gates. The surface wave interference-based all-optical logic could be realized when the conditions for the formation of BSW constructive/destructive interference can be fulfilled. The proposed all-optical logic was realized by controlling the BSW interference from high-intensity broadside radiation emitted by near-zero-index waveguide on the BSW platform. The working principle of the proposed logic gate is introduced in the following section.

Chapter 4 : Slab-guided BSW based chiral-metasurface for light switching

4.1 Introduction

As PICs include more individual optical elements and realize more complex functions, the ability to control the propagation direction of light is becoming important. Light switching based on spin-controlled unidirectional coupling has been demonstrated in chiral photonic circuits [67]. Spin-controlled unidirectional coupling is a phenomenon where circularly polarized light is coupled to guided waves with a specific propagation direction that depends on the spin of the light [68]. In an analogy to the quantum spin of electrons, circularly polarized light can be seen as composed of photons that possess a spin angular momentum whose sign depends on the handedness of the light, namely, either right-handed circular polarized (RCP) or left-handed circular

polarized (LCP). Spin-controlled waveguiding of SPPs arising in evanescent waves have been studied widely in recent years [69–72]. Chiral-sensitive metasurfaces, as two-dimensional nanostructures composed of subwavelength elements that can arbitrarily control the propagation direction of electromagnetic waves through spin-controlled coupling, have shown high directional selectivity in the unidirectional excitation of SPPs [41,73,74]. One of the studies demonstrated the light switching realized by SPP-based chiral-metasurface is shown in Figure 4-1 [41]. A subwavelength line aperture in a metal film enables incident light that is coupled into SPP that is polarized perpendicular to the light aperture. The emission pattern of the coupled SPP from the subwavelength line aperture is approximate to that of an in-plane electric dipole as shown in the inset of Figure 4-1(a). When many electric dipoles are arranged in a column, the column would launch plane wave SPPs that propagate away toward either side of the column under illumination as shown in Figure 4-1(a). The SPP plane wave source that is realized, the propagation of the plane wave depends on the polarization direction of light. When two of the columns are arranged as the column pair, the interference of the SPP plane wave emitted by each column would result in SPP plane waves propagates toward two sides with a different intensity which depends on the polarization state of the incident light as shown in Figure 4-1(b). The column-pair would emit SPP plane wave to the left when under LCP illumination and emit SPP plane wave to the right when under RCP illumination. To enlarge the intensity ratio between SPP plane wave propagate to right and the propagate to left, the multiple column-pair are arranged to enhance the interference of SPP as a complete chiral-metasurface as shown in Figure 4-1(c). The experimental result that demonstrated the light switching by the chiral-metasurface is shown in Figure 4-1(d) and (e). The near-field scanning optical

microscope image shows the intensity of SPP on the right side is much higher than that of on the left side under RCP illumination and vice versa.

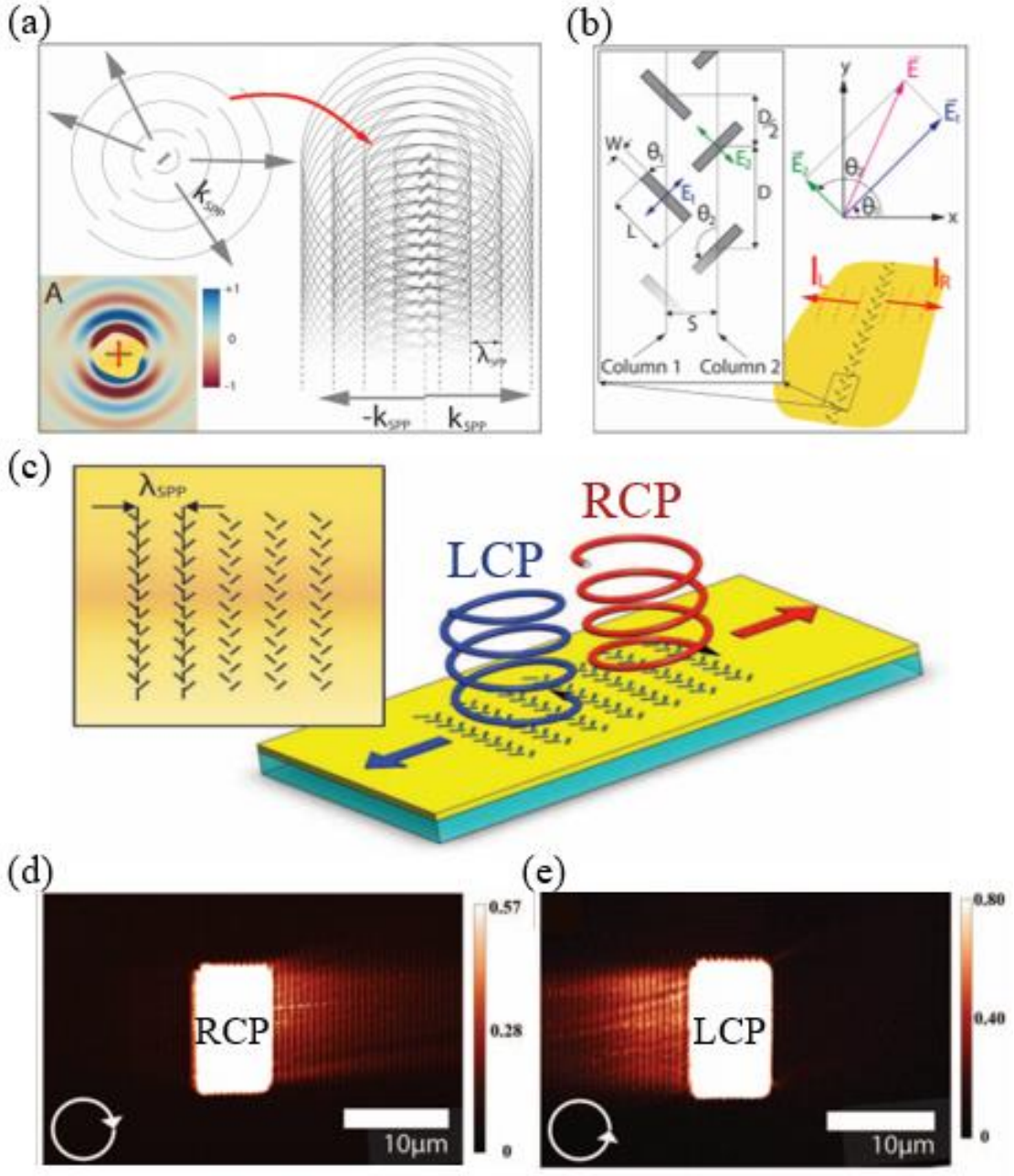

Figure 4-1 Closely spaced subwavelength apertures as polarization-selective SPP plane-wave sources. Inset of (a): The calculated normal component of the SPP electric field launched by an in-plane dipole (in arbitrary units), which is an approximation for a subwavelength aperture in a gold film (overlay) that is scattering incident light polarized perpendicular to its long axis (polarization indicated by a red arrow). (a) The SPP waves

generated by a single aperture propagate radially away from it, with wavefronts shown in black. The waves emitted from many apertures arranged in a column with subwavelength spacing interfere constructively along planes parallel to the column, shown as dashed lines. SPP wave vectors (k_{SPP}) are shown as gray arrows. (b) Two columns of apertures (1 and 2) are positioned in parallel with spacing S. The columns couple to the field components E_1 (blue arrows) and E_2 (green arrows) of the incident field E (pink arrow). The resulting combined SPP plane waves propagating away from the column pair (red arrows) have intensities I_R and I_L. (c) Multiple parallel column pairs are spaced λ_{SPP} apart. The structure is shown such that the right (left) CPL is coupled to the right (left) when it is incident from the top. Near-field scanning optical microscope images of the structure under illumination from the back by (d) RCP and (e) LCP light [41].

The ability to control the propagation direction and the operating wavelength of such structures through their shape and period makes them highly flexible. They, therefore, have the potential to facilitate the development of complex optical systems and PICs. However, SPP-based devices are limited in their practicality because of the short propagation lengths of SPPs, the narrow resonance wavelength ranges over which SPP devices operate, and the low-quality resonances of SPP devices caused by ohmic losses in their metal layers [75]. Although these devices offer only limited propagation lengths, relatively high directional selectivity for the unidirectional excitation of SPPs on metasurfaces has been achieved [42].

Recently, BSWs have been applied in photonic device components [26,76] and sensors [77]. While the coupling, propagation, and sensing properties of BSWs have been investigated extensively, studies on the use of BSWs in chiral optic devices are limited. Only a limited directional BSW excited by a single groove has been

reported [78], and the directional selectivity was relatively low (≈7 dB) compared to SPP-based chiral optic devices which have demonstrated directional selectivities up to 11 dB [73]. Although the near-field unidirectional coupling of the surface wave on 1D-PC has been demonstrated in simulation, the design still contains a metal top layer which causes the propagation loss to be very high [79]. The study of metal-free chiral-sensitive metasurfaces on a dielectric multilayer BSW platform remains unexplored. In this study, we experimentally demonstrate a metal-free chiral-sensitive BSW switching circuit that couples incident light to a BSW with a polarization-dependent propagation direction. The propagation of a guided BSW mode with a propagation length of approximately 135 μm along a thin (40 nm) subwavelength guiding slab is first demonstrated. The preferential coupling of incident light to guiding slabs on the left or right of the metasurface based on the handedness of the incident light polarization is then shown. The metasurface is optimized to have a directional selectivity (ratio of the electric field intensity propagating in the guiding slab on the right to the slab on the left) of 23 dB when illuminated by LCP light in simulation. In experiment, the design is found to have a directional selectivity of 13 dB. The strong directional selectivity of the BSW switching chiral-sensitive metasurface demonstrates its ability to manipulate the propagation direction of electromagnetic surface waves on a metal-free 1D-PC BSW platform. It is believed that this metal-free chiralsensitive BSW switching circuit is a promising tool in a variety of applications such as optical circuit and chirality-related devices.

4.2 Design of chiral-metasurface on BSW platform

4.2.1 Investigation of chiral-metasurface on BSW platform

The possibility for spin-controlled light switching on the BSW platform is investigated in the following. A U-shaped aperture (radius R = 450 nm and width = 200 nm) is used

as the unit element for the chiral-sensitive metasurface. Figure 4-2 shows the real part of the out-of-plane magnetic field H_z distribution obtained from a single U-shaped aperture under illumination by linear polarized light of varying polarization angles. Because the incident light has no out-of-plane magnetic field H_z, this field component is used to investigate the behavior of the excited BSWs. When the aperture is excited by incident light, it behaves as an in-plane dipole source that launches BSWs. The launched BSWs propagate perpendicular to the polarization direction of light. This is different from SPPs launched by dipole sources, as they propagate parallel to the polarization direction of the light. Since the dipole source orientation depends on the polarization angle of the incident light, the phase and amplitude of the launched BSWs depend on the polarization angle as well. The arrangement of dipole sources enables the manipulation of the amplitude and phase of the BSWs, thus allowing for the excitation of unidirectional BSWs.

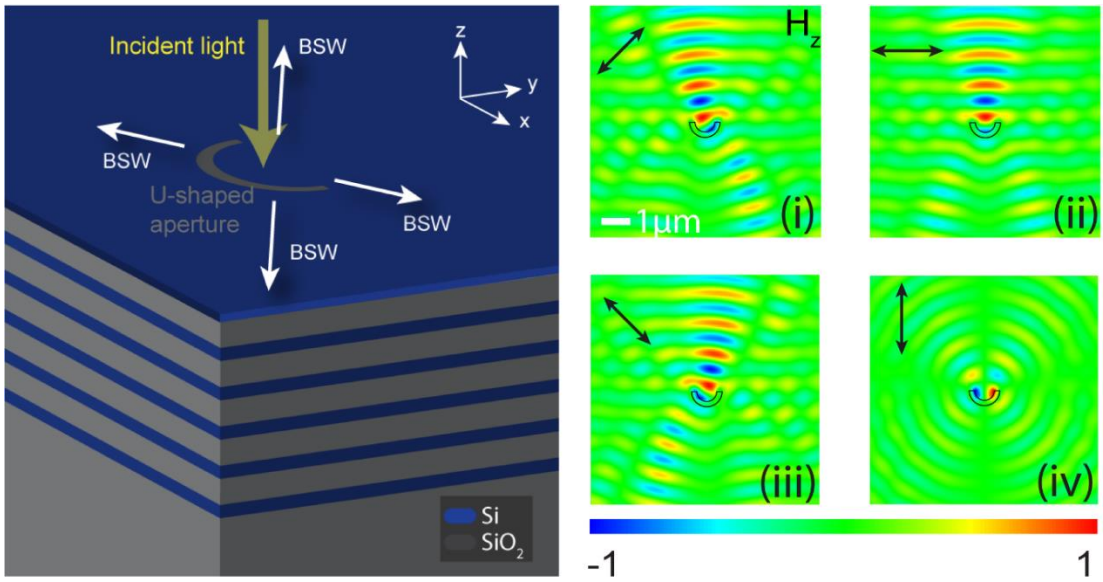

Figure 4-2 Design of the chiral-metasurface on the dielectric multilayer BSW platform. Real part of the magnetic field distribution H_z for a single U-shaped aperture under illumination by linearly polarized light of various angles. The polarization direction of the incident light in each figure is indicated by a black arrow

In order to obtain propagating BSWs with a flat wavefront, the U-shaped apertures are arranged in a column. The interference of BSWs coupled by each individual aperture results in BSWs with flat wavefronts that propagate on either side of the column. This is observed in the H_z distribution (Figure 4-3 (a),(e)) of the BSW excited by incident light with polarization angles of 45° ($BSW_{45°}$) and 135° ($BSW_{135°}$), respectively. The phase and amplitude of the rightward propagating BSW depend on the polarization angle as shown in Figure 4-3(c). By comparing the phase of H_z between $BSW_{45°}$ and $BSW_{135°}$, it can be seen that the leftward propagating $BSW_{45°}$ is ahead in phase by δ relative to $BSW_{135°}$ as shown in Figure 4-3(b). In the rightward propagating BSW, the phase difference is $-\delta$ as shown in Figure 4-3(d). When the incident light is LCP, there is a phase difference of $\pi/2$ between the incident light having a polarization angle of 45° and the incident light having a polarization angle of 135°. Therefore, the total phase (δ_{tot}) difference between the BSWs launched by LCP light at polarization angle of 45° and at the polarization angle of 135° is $\delta_{tot(left)} = (\pi/2) + \delta$ on the left side and $\delta_{tot(right)} = (\pi/2) - \delta$ on the right side.

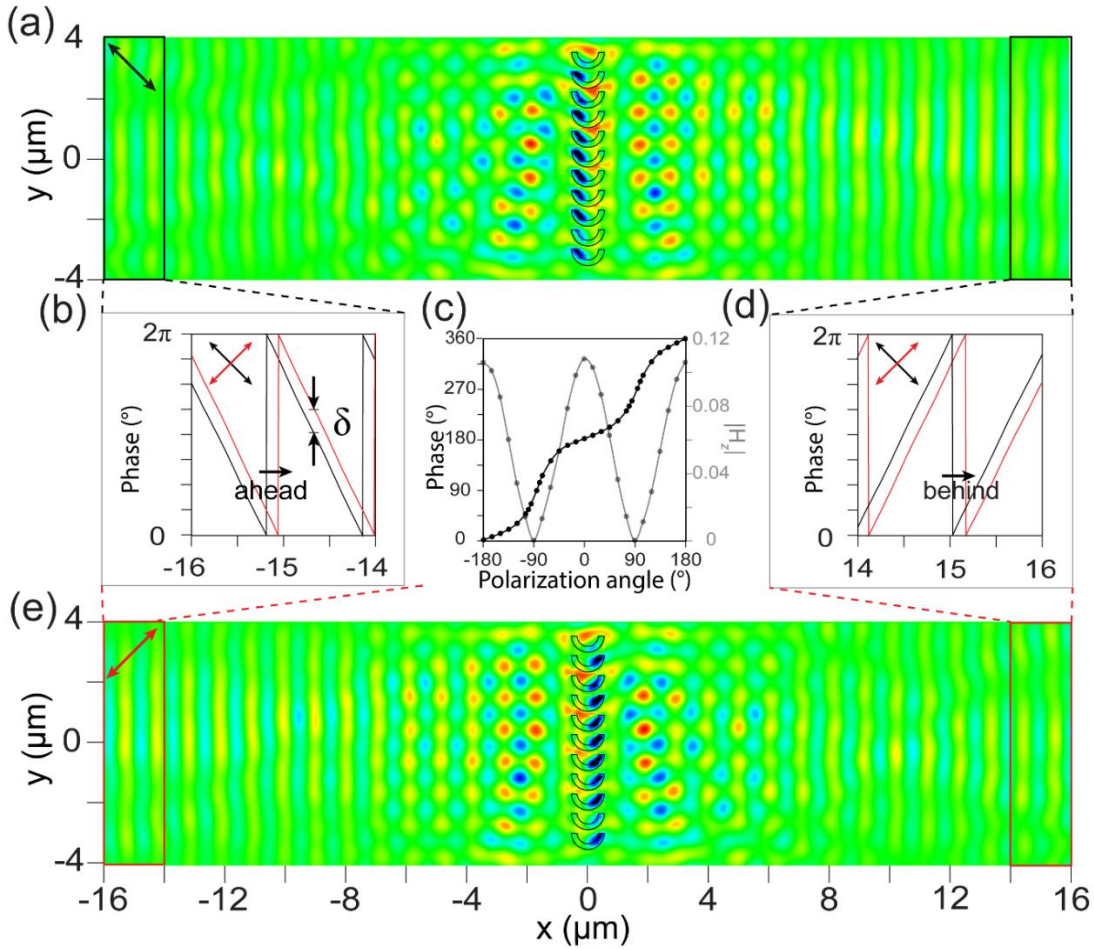

Figure 4-3 Real part of the magnetic field distribution, Hz, for a single column of U-shaped apertures under illumination by light with (a) 45° linear polarization, (e) 135° linear polarization. The phase variation of H_z from (b) x = -14 to -16 (left) and d x = 14 to 16 (right) for y=0. (c) Dependence of the phase and amplitude of H_z on the polarization angle at the position x = 15, y = 0 when a U-shaped aperture column is illuminated by linearly polarized light.

When δ is between 0 and π, BSWs propagating to the left of the column undergo partial destructive interference, and those to the right undergo partial constructive interference, giving preferential excitation of the rightward propagating BSW when the U-shaped aperture column is illuminated by LCP light (Figure 4-4(a)). When the U-shaped aperture column is illuminated by RCP light, BSWs propagating to the right of the column undergo partial destructive interference, and those to the left undergo partial

constructive interference, giving preferential excitation of the leftward propagating BSW as shown in Figure 4.4(b).

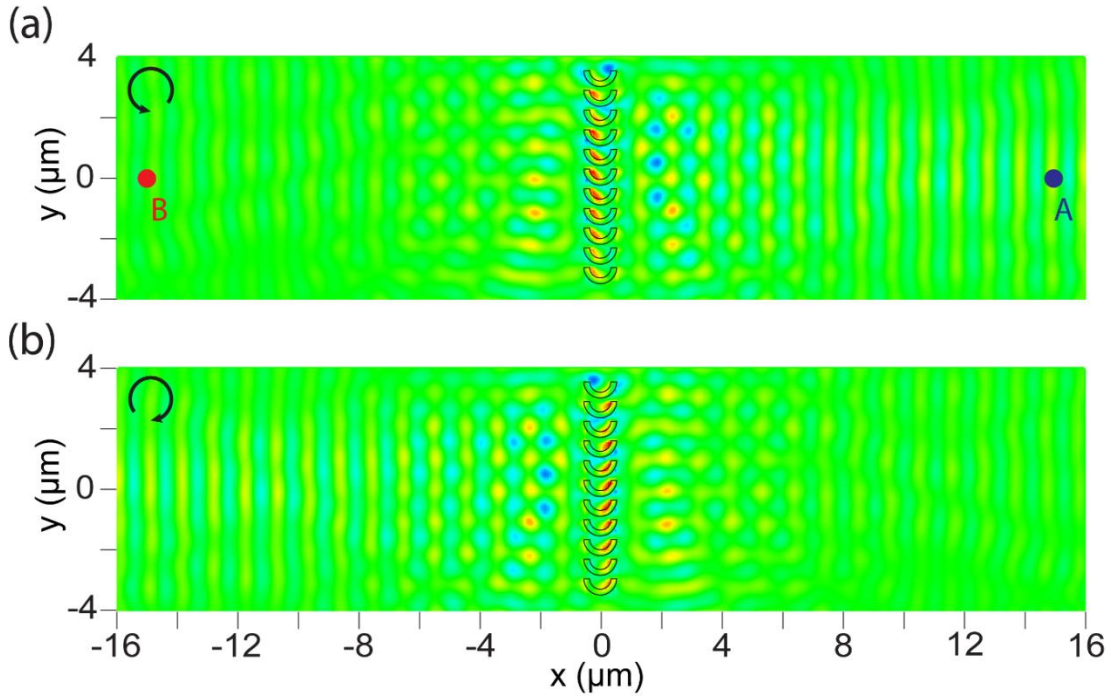

Figure 4-4 Real part of the magnetic field distribution, H_z, for a single column of U-shaped apertures under illumination by light with (a) LCP and (b) RCP.

To better understand how high directional selectivity is achieved with the U-shaped aperture column, an analysis of the BSWs launched by LCP light is performed as shown in Figure 4-5. The phase and amplitude of BSWs at reference positions of x = 15 and −15 μm and y = 0 μm (Points A and B in Figure 4-4(a)) can be modeled as sine waves. To model the BSWs excited by LCP light, the sine waves of each polarization angle are shifted by specific amounts corresponding to the phase at which LCP light has the given polarization angle. These sine waves are plotted as colored curves in Figure 4-5(a) (Point B) and Figure 4-5(b) (Point A). The sine waves propagating to the right (Figure 4-5(b), blue inset) are more in-phase than the sine waves propagating to the left (Figure 4-5(a), red inset). The sine waves are summed to give the net BSWs propagating to the left and to the right of the aperture column as shown in the black curve in Figures 4(a)

and (b). The interference of the BSWs coupled by the different polarization angles results in the rightward propagating light having a higher intensity than the leftward propagating light. This explains why the U-shaped aperture column couples LCP light preferentially to the rightward propagating BSW as seen in Figure 4-4(a). Note that this result explains the concept of unidirectionally excited BSW by using a single column of U-shaped apertures. An array of U-shaped apertures realizing the BSW with high directional selectivity is demonstrated in the next paragraph.

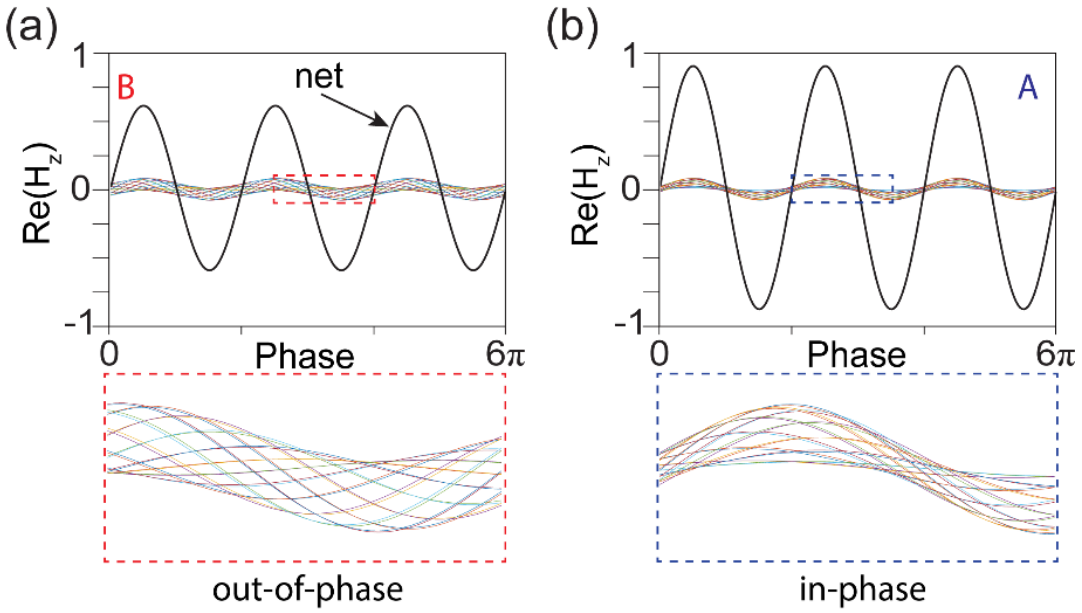

Figure 4-5 Variation of the real part of the magnetic field (Re (H_z)) with the phase at (b) Points A and (a) B (indicated in Figure 4.4(a)). The interference of BSWs launched by all components of LCP light (colored lines) results in the propagating BSW on the right having a higher intensity than the propagating BSW on the left, as shown by the net H_z (black line). Inset: Zoomed-in plot of the H_z of the BSWs launched by all components of the LCP light.

4.2.2 Optimization of chiral-metasurface on BSW platform

To improve the directional selectivity, the interference effect is enhanced by arranging multiple U-shaped aperture columns into an array to form a chiral-sensitive metasurface as shown in Figure 4-6(a). To optimize the chiral-sensitive metasurface, the normalized electric field energy density distributions to the right of the metasurface E_R and to the left of the metasurface E_L are examined as shown in Figure 4-6(b). 3D FDTD simulations are performed for normally incident LCP light, and the electric field ratio $|E_R|^2/|E_L|^2$ is optimized by varying four parameters, namely, the vertical period P_M, horizontal period P_N, row number M, and column number N. Figure 4-6(b) shows the variations of the electric field extinction with the four parameters and indicates the optimized parameters as red dots. Note the increase in the electric field extinction as the parameters are being optimized. First is the vertical period P_M, it was optimized to be 0.65, which is very close to half of λ_{BSW}. The horizontal period P_N was then be optimized with the fixed vertical period P_M, the horizontal period P_M was optimized to be 1.3, which is very close to λ_{BSW}. The third parameter is the number aperture in a column M, the BSW plane wave can not be formed with too fewer apertures in a column, but too many apertures in a column will disturb the formation of a plane wave, the number of apertures in a column was optimized to be 7. For the last parameter, the number of columns N, the directional selectivity is increased with the increase of the number of columns due to the more surface waves with the same phase, which enhance the interference, resulting in larger directional selectivity as shown in the black dots. But since the fixed spot size of the incident light, only the limited area (the diameter of spot size was set to be 10 μm) of chiral-metasurface will be used to couple BSW, the output energy is decreased with the increased of column numbers as shown in grey dots. Therefore, the number of columns is optimized to be 15.

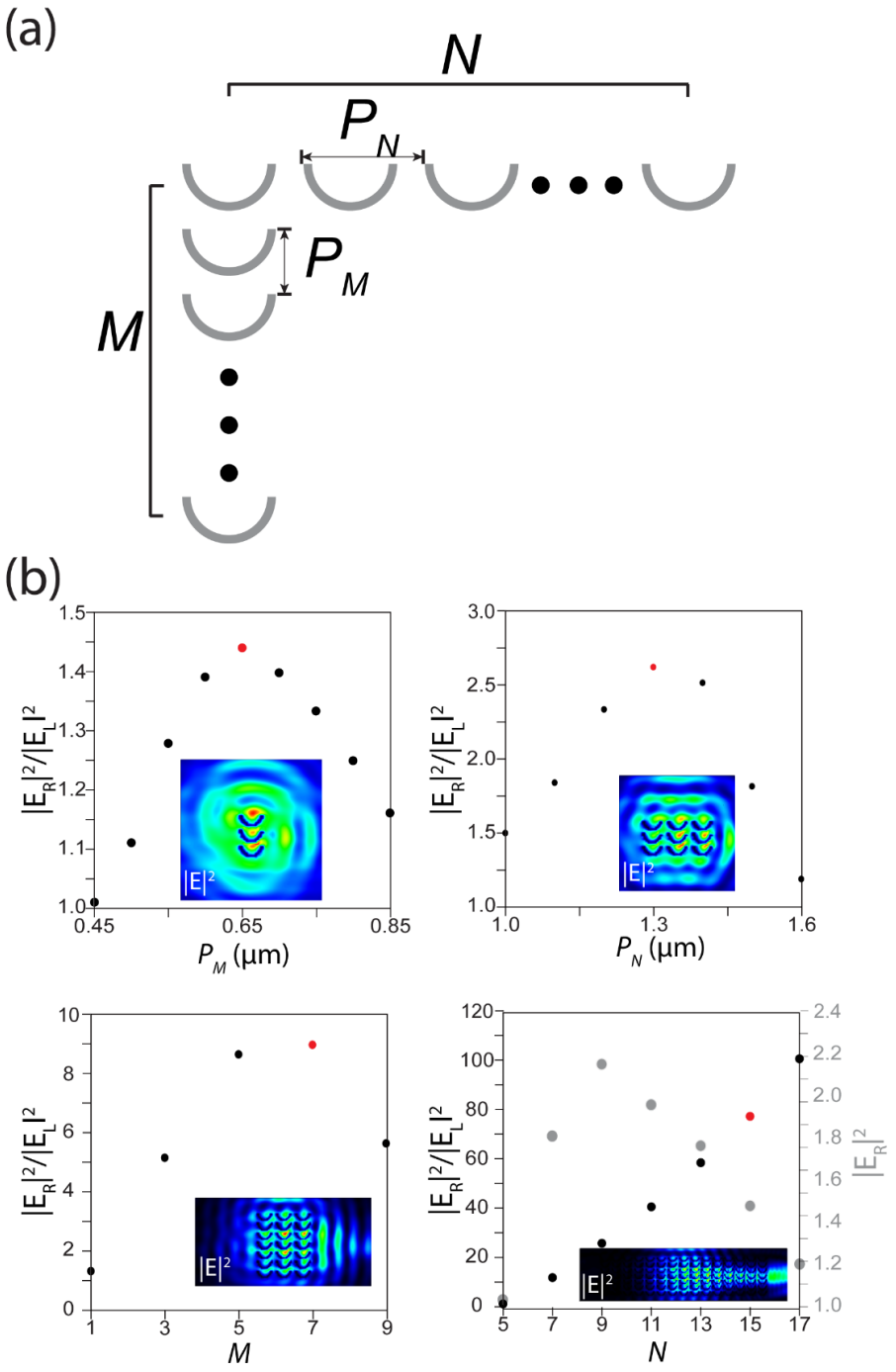

Figure 4-6 (a) Schematic design of the BSW chiral-sensitive metasurface indicating the vertical period P_M , horizontal period P_N, number of apertures in a column M, and number of apertures in a row N. (b) The electric field energy density extinction ratio of the U-shaped apertures under illumination by LCP light for four varying parameters a P_M, b P_N, c M, and d N. Insets are the electric field intensity distributions in the xy-plane for the conditions indicated by the red dots.

4.2.3 Characterization of chiral-metasurface on BSW platform

Figure 4-7(a) shows the normalized H_z intensity distribution in the metasurface under illumination by LCP light. Due to constructive interferences on the right side, the H_z intensity on the right side becomes much stronger than on the left side. Moreover, Figure 4-7(b), which shows that the H_z phase distribution reveals phase discontinuities on the left side and well-formed wavefronts on the right side. Note that the guiding slab that supports the guided BSW is connected to the metasurface at the position of the phase discontinuities to further improve the directional selectivity.

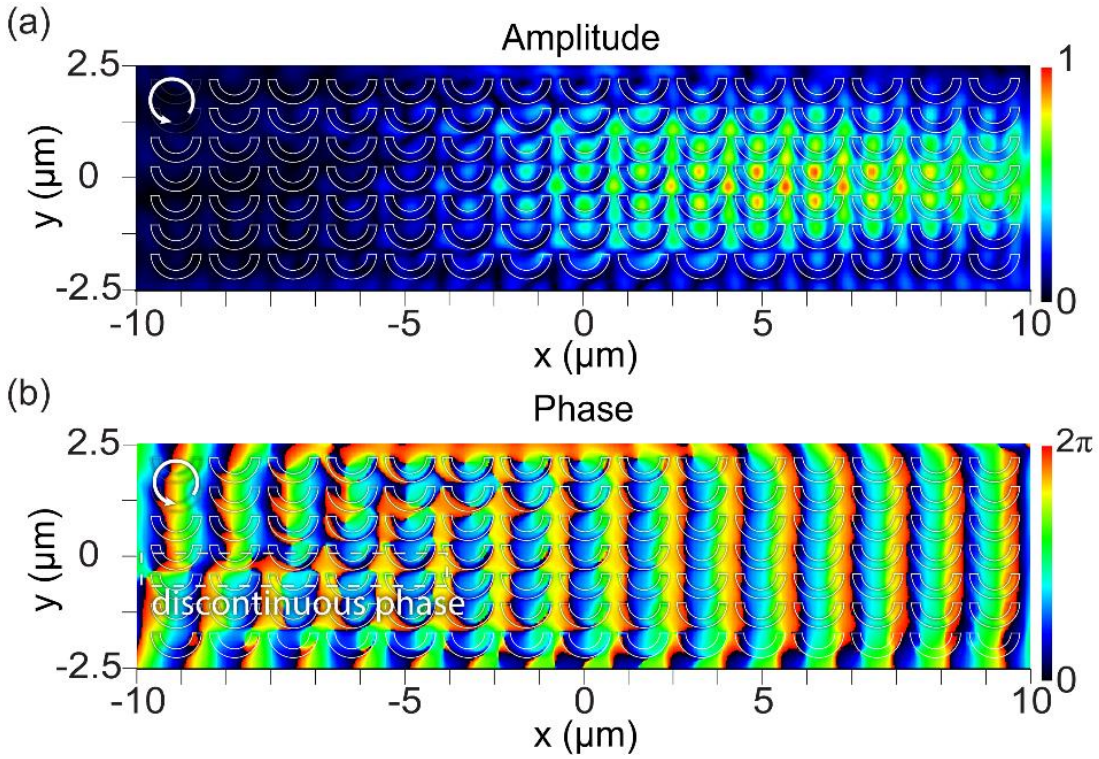

Figure 4-7 Simulated results of the chiral-sensitive metasurface on the 1D-PC BSW platform under LCP light illumination. Normalized magnetic field H_z (a) amplitude and (b) phase distribution of H_z over the chiral-sensitive metasurface in an x−y plane through the center of the top layer.

The chiral-sensitive BSW switching circuit consisting of the U-shaped aperture array (chiral-metasurface) connected to two guiding slabs and grating couplers on the 5-pair Si/SiO_2 dielectric multilayer BSW platform is investigated in the following. Figure 4-8(a), (b), and (c) show the normalized electric field energy density $E_{density}$ distribution of the circuit under illumination by TE-polarized, LCP, and RCP light, respectively, in simulations. A Gaussian beam is used to launch the polarized beam onto the center of the chiral-sensitive metasurface. For the case of TE-polarized light, the incident light is coupled with equal intensities into guided BSWs propagating in the guided slabs on the left and right of the metasurface, as shown in Figure 4-8(a). Figure 4-8(b) and (c) show the simulated results for circularly polarized light with left- and right-handedness, respectively. The propagation direction of the BSWs coupled by the metasurface is controlled by the spin of the incident light, with a directional selectivity greater than 20 dB.

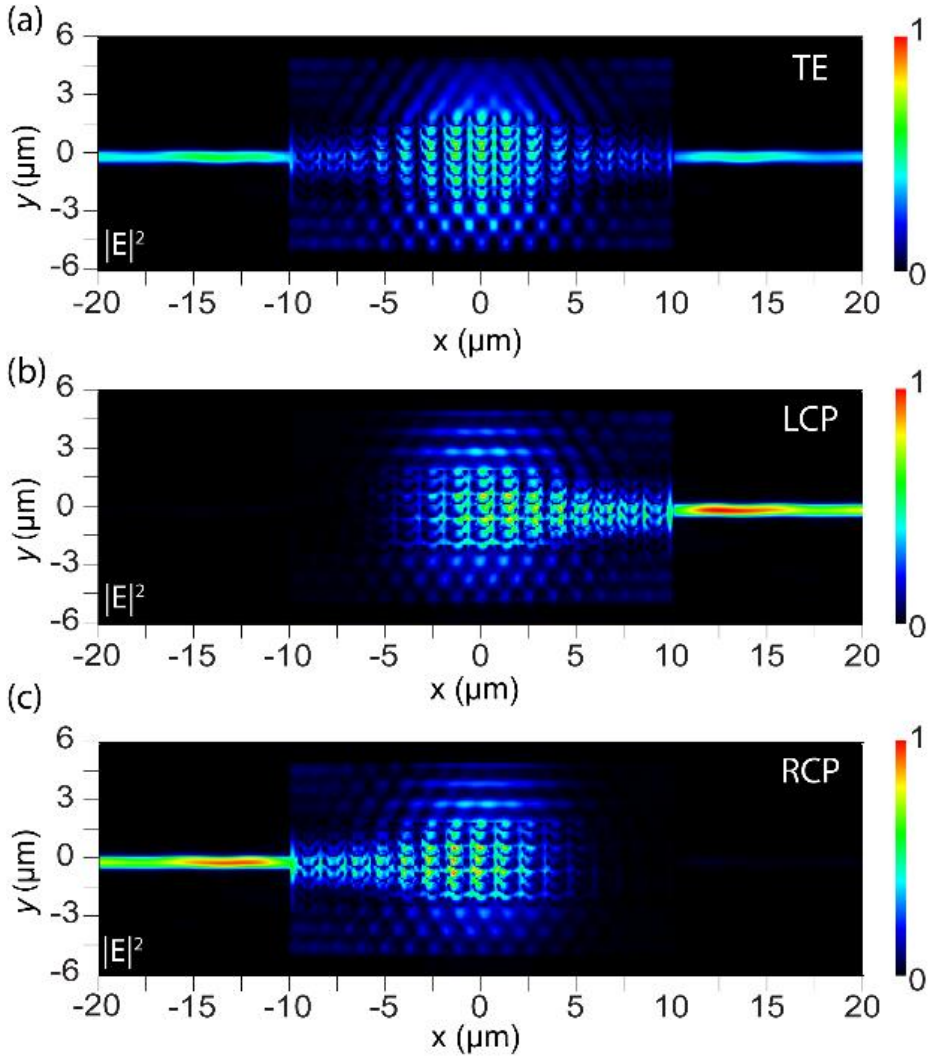

Figure 4-8 Simulated results of the chiral-sensitive metasurface on the 1D-PC BSW platform under LCP light illumination. Normalized magnetic field H_z (a) amplitude and (b) phase distribution of H_z over the chiral-sensitive metasurface in an x−y plane through the center of the top layer.

4.3 Working principle of slab-guided BSW based chiral-metasurface for light switching

The structure and working principle of the metal-free chiral-sensitive BSW switching circuit are illustrated in Figure 4-9. This metal-free chiral-sensitive BSW switching circuit (Figure 4-9(a)) consists of a central chiral-metasurface with guiding slabs on two sides of the chiral-metasurface and coupling gratings at the ends of the slabs, all on top of a 5-pair Si/SiO_2 dielectric multilayer BSW platform. The chiral-metasurface enables the control of the BSW propagating direction. When this metasurface is illuminated by TE-polarized, LCP, and RCP light, the excited BSW is found to propagate on both sides, the right side only and the left side only, respectively (Figure 4-9 (b−d)). The BSW can be guided through guiding slabs connected to the metasurface on the left and right sides and coupled out by the grating couplers that are located at the ends of the guiding slab, as shown in Figure 4-9(a).

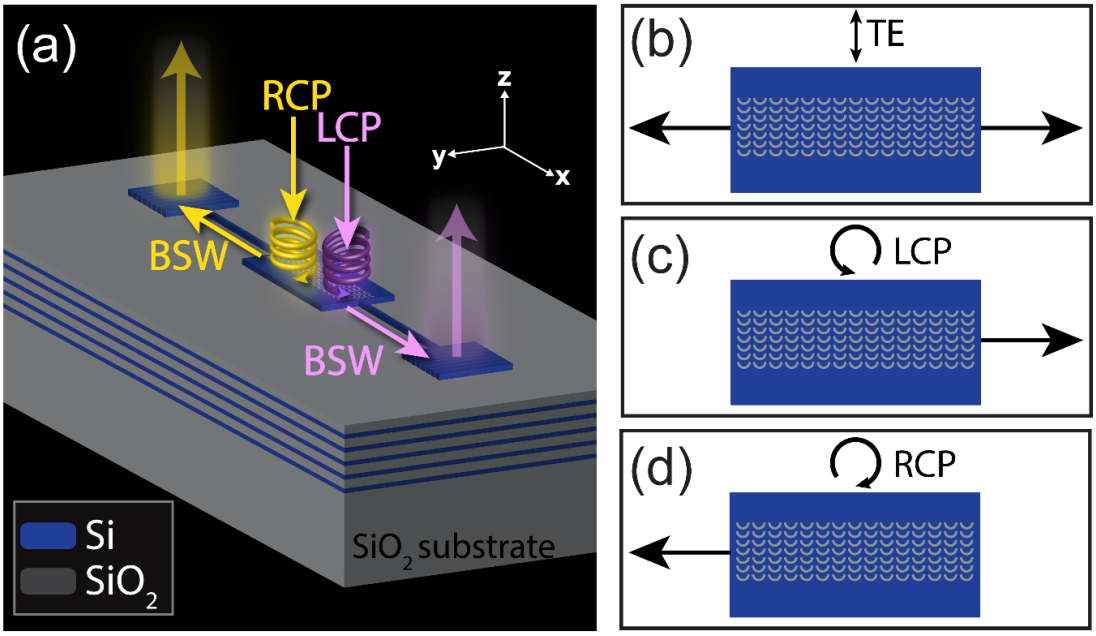

Figure 4-9 Working principle of the slab-guided BSW-based chiral-metasurface light switching circuit. (a) The schematic illustration of the chiral-metasurface BSW light switching circuit. Yellow and purple arrows on the sample denote the direction that the

BSW propagates when the chiral-metasurface is illuminated by normally incident RCP light and LCP light. Schematic illustration of the metasurface launches BSWs on (b) both sides of the metasurface for TE-polarized incident light, (c) the right side for LCP incident light, and (d) the left side for RCP incident light

4.3 Fabrication and Characterization of slab-guided BSW based chiral-metasurface light switching circuit

The fabrication process is the same as that of in Chapter 2. Si and SiO_2, with thicknesses of 190 and 378 nm, respectively, were deposited on a SiO_2 substrate using a RF-magnetron sputtering system (CFS-4ES, Shibaura Engineering Works Co., Ltd., Yokohama, Japan). Metasurface, guiding slab, and grating coupler patterns were defined by electron beam (EB) lithography. The electron beam resist (ZEP520A, Zeon Corporation, Tokyo, Japan) was spin-coated at 3000 rpm with a thickness of about 400 nm. The exposure dose of the electron beam system (F7000SVD02, Advantest, Tokyo, Japan) was set to 104 μC/cm2. The development was performed using n-amyl acetate as a developer and methyl isobutyl ketone and isopropyl alcohol for rinsing. The Si top layer with a thickness of 40 nm was deposited on top of the patterned resist. The lift-off process removed the resist with Si top layer. Dimethylacetamide was used as a stripper in the lift-off process. The process was done at room temperature. The fabricated sample as shown in the SEM and optical microscope images in Figure 4-10

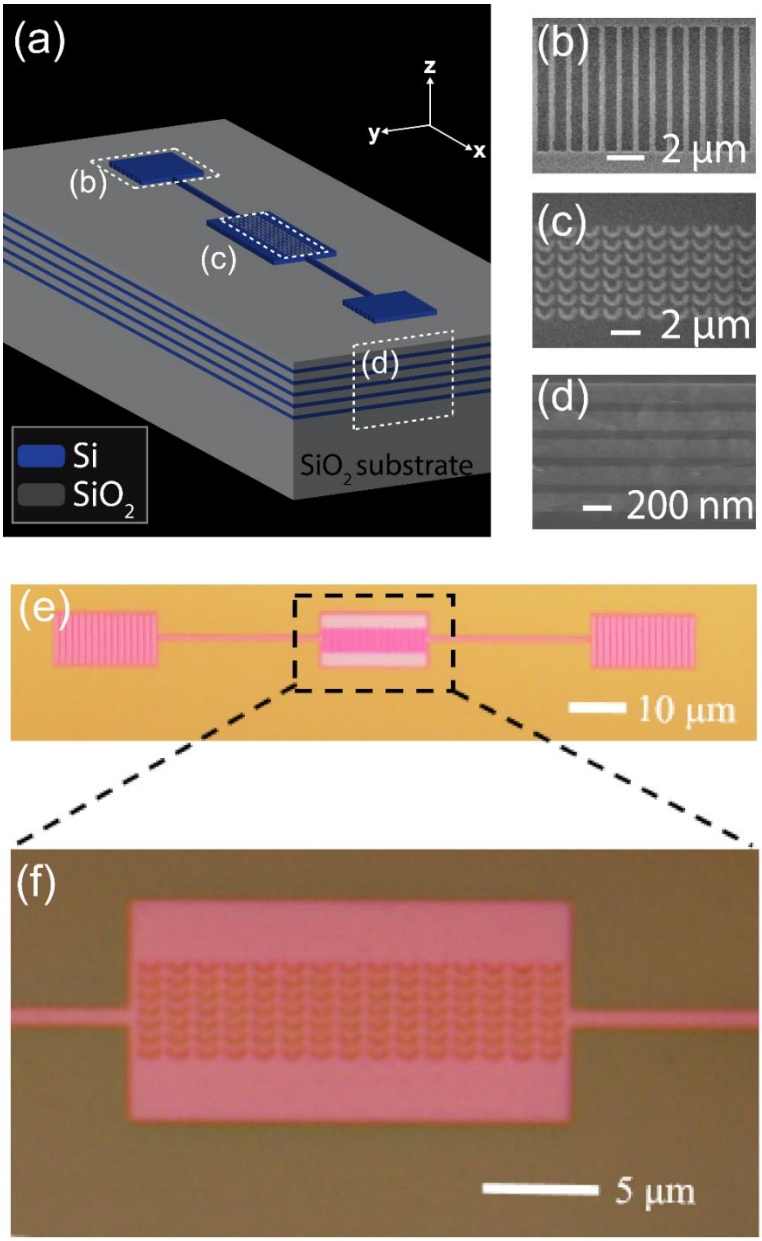

Figure 4-10 (a) The schematic illustration of the slab-guided BSW based chiral-metasurface light switching circuit. SEM images of (b) the grating coupler, (c) the chiral-metasurface, and (d) the cross-section of the Si/SiO_2 dielectric multilayer BSW platform. Optical microscope image of (e) the chiral-metasurface BSW light switching circuit and (f) the chiral-metasurface.

The corresponding experimental results obtained from the fabricated slab-guided BSW-based chiral-metasurface light switching circuit are shown in Figure 4-12(a), (b) and (c) for TE-polarized, LCP, and RCP incident light, respectively. The evaluation was

conducted using the setup as shown in Figure 4-11 where the quarter-wave plate was used to generate LCP and RCP incident light that was focused onto the center of the metasurface by the objective lens. The IR camera captures images of the light reflected by the metasurface and out-coupled by the coupling gratings on either side of the metasurface

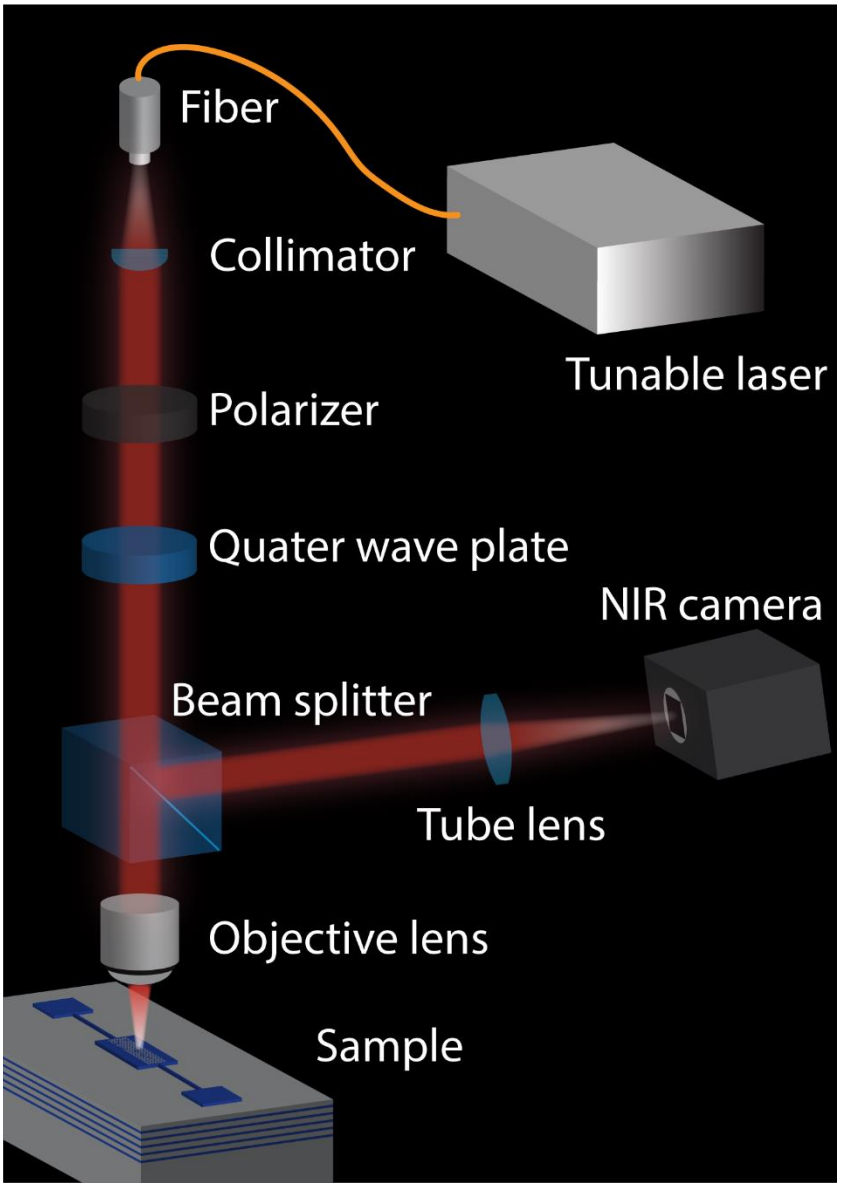

Figure 4-11 Experimental setup used to couple incident light to a guided BSW and collect the out-coupled light. Incident light is TE-polarized, LCP, or RCP by using polarizer and quarter wave plate. The polarized light focused onto the in-coupling

grating, and the excited BSW propagates along the guiding slab until reaching the out-coupling grating where it is decoupled, collected by the objective lens, and imaged by the NIR camera.

The integrated intensity of the out-coupled light from the left and right coupling gratings we calculated for the three cases above and are compared in Figure 4-12. When the chiral-sensitive metasurface is excited by incident TE-polarized light, the intensities are nearly the same, and the ratio of the intensity from the coupling grating on the right to that on the left is 1.09. In the case of LCP light, however, the ratio is as high as 22.56, which corresponds to a directional selectivity of the rightward propagating BSW over the leftward propagating BSW of 13.53 dB. When the illuminating light is RCP, the directional selectivity is −13.15 dB (the negative indicates that the leftward propagating BSW is stronger for RCP light). The difference in the directional selectivity between the computed and experimental values originated in imperfections in the fabrication of the U-shaped aperture and also in the nonideality of the illumination (actual laser spot) of the structure array. These observed directional selectivities are higher than values reported in the literature (10 dB or less) for SPP-based spin-controlled unidirectional launchers [44,73]. By changing the rotation angle of the quarter-wave plate used to create the circularly polarized light, the directional selectivity of the chiral-sensitive BSW switching circuit was measured for a variety of elliptical polarization as shown in Figure 4.12(e). LCP and RCP light is obtained for rotation angles of +45° and −45°, respectively. When the rotation angle is close to either 45° or −45°, the magnitude of the directional selectivity reaches a maximum. On the other hand, for rotation angles of −90°, 0°, and 90°, where the incident light is TE-polarized, the directional selectivity is 0 dB (intensity on the left and right are the same). The observed change in the directional selectivity indicates a continuous variation of the polarization state from linear

polarization to elliptical polarization, LCP, elliptical polarization, linear polarization, elliptical polarization, and RCP. Such a tunable polarization state enables arbitrary control of the intensity of light coupled into PICs. It is worth noting that this represents the first demonstration of spin-controlled surface wave switching using a metal-free chiral-sensitive metasurface.

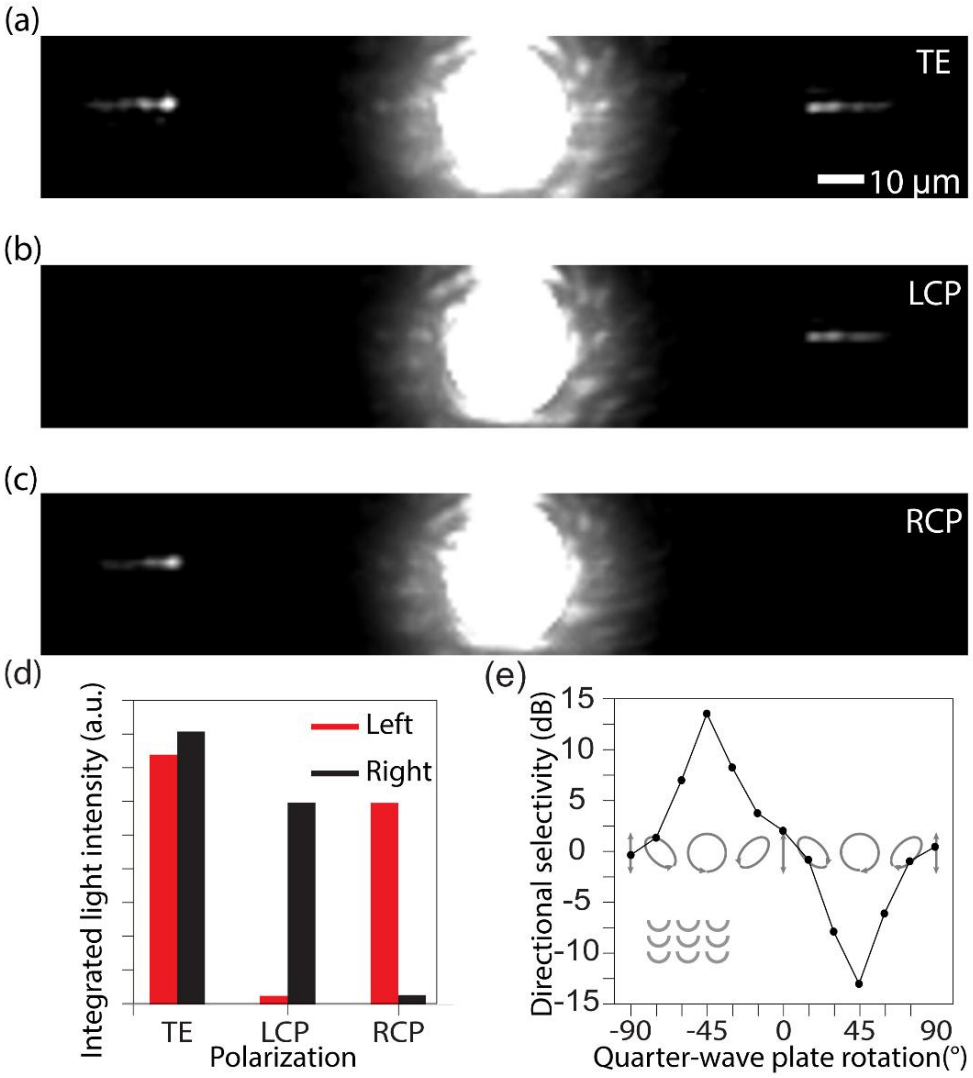

Figure 4-12 NIR images of the fabricated chiral-metasurface with guiding slabs and output couplers attached to the ends of the guiding slabs under illumination by (a) TE polarized, (b) LCP, and (c) RCP light. Spots in the center of the images show the reflection of incident light from the chiral-metasurface and the spots on the left and right

show the light guided by the guiding slabs being out-coupled from the coupling gratings at the ends of the guiding slabs. (d) Integrated light intensities of out-coupled light from the left and right coupling gratings for TE-polarized, LCP, and RCP incident light. (e) Directional selectivity of light out-coupled from the left and right coupling gratings plotted against the rotation angle of the quarter-wave plate used to polarize the incident light (rotation angles of −90°, −45°, 0°, 45°, and 90° correspond to TE polarization, LCP, TE polarization, RCP, and TE polarization, respectively).

4.4 Discussions

In summary, we have theoretically predicted and experimentally demonstrated a metal-free chiral-sensitive BSW switching circuit by carefully arranging an array of U-shaped apertures. We experimentally demonstrated guided BSW propagation along an ultrathin (40 nm thickness) guiding slab having a propagation length of 135 μm. The proposed chiral-sensitive metasurface is used to control the propagation direction of guided BSWs based on the chirality of incident light. At a wavelength of 1550 nm, directional selectivity is as high as 23 dB theoretically and 13.53 dB experimentally. The ability to realize spin-controlled light switching on a chip at telecommunications wavelengths using the chiral-sensitive metasurface makes it promising for applications in low-loss on-chip photonic integrated devices and sensors. The comparison table of this work and the previous works of light switching devices as shown in Table 4.1. The first SPP-based light switching based on metal chiral-metasurface has been demonstrated in 2013 by Lin et al [41]. The propagation length of the light switching device is around only 10 μm due to the ohmic loss from metal layer. The directional selectivity of the light switching device is demonstrated with around 8 dB. The nanoslit array SPP-based light switching device has been demonstrated with much higher directional selectivity up to 12.48 dB [73], but the propagation length is still limited as the issue of the SPP-based

device. The BSW-based light switching has been demonstrated with much longer propagation length which is up to 120, but the directional selectivity is quite low (~7) due to the poor chiral sensitivity of the simple grove structure [78]. In this work, thanks to the metal-free and high chiral sensitive metasurface, the propagation length is as long as 135 μm and the directional selectivity is as high as 13.53 dB.

Table 4.1: Summary of the light switching devices

Structure	**Operating wavelength (μm)**	**Propagation length (μm)**	**Directional selectivity (dB)**	
SPP-based chiral-metasurface	0.633	10	~8	Lin et al. *Science*, (2013) [41]
SPP-based nano-slit array	0.671	<10	12.48	Qiao et al. *Advanced Functional Materials*, (2018) [73]
Grove structure on BSW platform	1.55	~120	~7	Mengjia et al. *Light: Science & Applications*, (2018) [78]
Metal-free chiral-metasurface on BSW platform	**1.55**	**135**	**13.53**	**Deng et al. ACS photonics (2020)**

Chapter 5 : Two-pair Ge/SiO_2 dielectric multilayer BSW platform

5.1 Introduction

The BSW-based applications have been widely studied as mention in Chapter 1. However, most of these BSW platforms require a large number of alternating layers (more than six-pair multilayer) [20,21,24–27,80,81] to realize the coupling of the surface mode due to the small difference of refractive index between high- and low-refractive-index material. Additionally, although BSW modes have been investigated in the visible region [26] and the near-infrared (NIR) region [39,80] very few reports are available for the mid-infrared (MIR) region [82]. MIR spectroscopy enables the determination of characteristic vibrational resonances of many functional molecules so that it can be used to perform label-free sensing [83], medical diagnostics [84], and food analysis [85]. Therefore, a BSW platform that works in the MIR region with a few numbers of alternating layers is a promising candidate for the surface wave application in the MIR region.

5.2 Design of two-pair Ge/SiO_2 multilayer BSW platform

To design the multilayers that match the conditions for BSW, the thicknesses of the high and low refractive index layers *d* are calculated based on the forbidden transmission band at the target wavelength λ of 1DPC bandgap material,

$$d = \frac{\lambda}{4n\cos\theta}$$

where n is the refractive index and θ is the propagation angle of light within the high and low refractive index layers, respectively. The 2D Rigorous coupled-wave analysis (RCWA) simulations with the conditions of TE-polarized incident into the Ge/SiO_2 multilayer at different wavelengths and incident angle are performed. Figure 5-1 shows

the band diagram of the proposed Ge/SiO_2 multilayer. The BSW mode represented by the red line falls in the forbidden band, and the red circle on the red line indicates the TE-polarized incident light with the wavelength λ = 1550 nm and incident angle θ = 54.5°. The thicknesses of the multilayer are optimized with the low refractive index layer d_L = 310 nm, high refractive index layer d_H = 105 nm, and an additional top layer of Ge having a thickness d_T = 15 nm. The additional top layer is used to modify the maximum field enhancement from the low-refractive-index layer to the top of the surface of the dielectric multilayer.

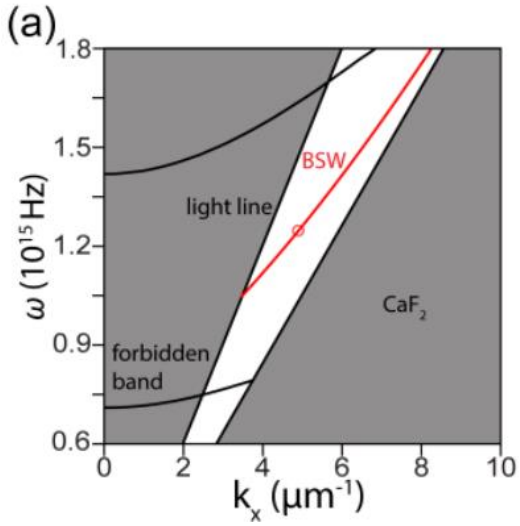

Figure 5-1 The dispersion diagram of the Ge/SiO_2 BSW multilayer

Since the resonance wavelengths of BSWs are determined by the thicknesses of the multilayer, BSWs in the MIR region can be achieved by varying the layer thicknesses. BSWs with different resonance wavelengths are obtained by varying the layer thicknesses for fixed ratios between d_H d_L, and d_T. The additional layer on top of the multilayer enable strong BSW coupling at top surface. In contrast to the multilayer without the additional top layer having the maxima of the electromagnetic (EM) field inside the low refractive index layer, the multilayer with the additional top Ge layer exhibits maxima inside the top layer. Moreover, the reflectance dip of the multilayer

with the additional top layer is much narrower than that without the additional top layer as shown in Figure 5-2 (a) and (b).

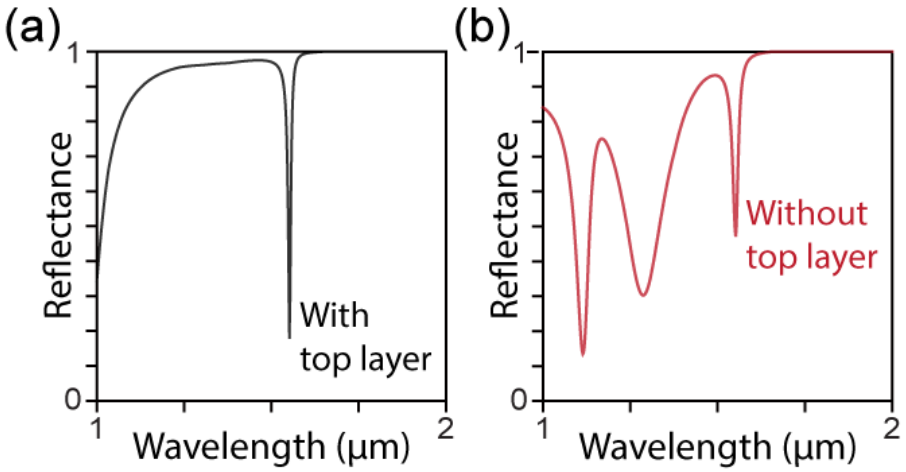

Figure 5-2 (a) Reflectance spectrum of the two-pair Ge/SiO_2 BSW multilayer with and without the top layer

We introduce the thickness multiplicative factor α to study the effect of the variation in the layer thicknesses for fixed thickness ratios and α = 1 corresponding to d_L = 310 nm, d_H = 105 nm, and d_T = 15 nm as shown in Figure 5-3. The low reflectance positions within the forbidden band indicate that the light is coupled into BSW mode and propagates on the surface. The BSW mode wavelength is red-shifted when α is increased can be observed in Figure 5-2 (a). The point A and B in Figure 5-2 are BSW modes that exist at NIR and MIR regions, respectively. For α = 1, there exists only one sharp dip at λ = 1550 nm corresponding to the BSW mode as shown in Figure 5-3(b). The reflectance spectrum shows a sharp dip with a full width at half maximum (FWHM) = 8.6 nm and a strong coupling of light with a minimum reflectance = 0.18. For α = 3 (d_L = 930 nm, d_H = 315 nm, and d_T = 45 nm), the reflectance results reveal a shift of the sharp-dip BSW mode to λ = 4280 nm and the presence of several high-order modes at shorter wavelengths. The reflectance spectrum shows the sharp dip that corresponding

to BSW mode with an FWHM = 12 nm and strong coupling of light with a minimum reflectance = 0.12 as shown in Figure 5-3 (c).

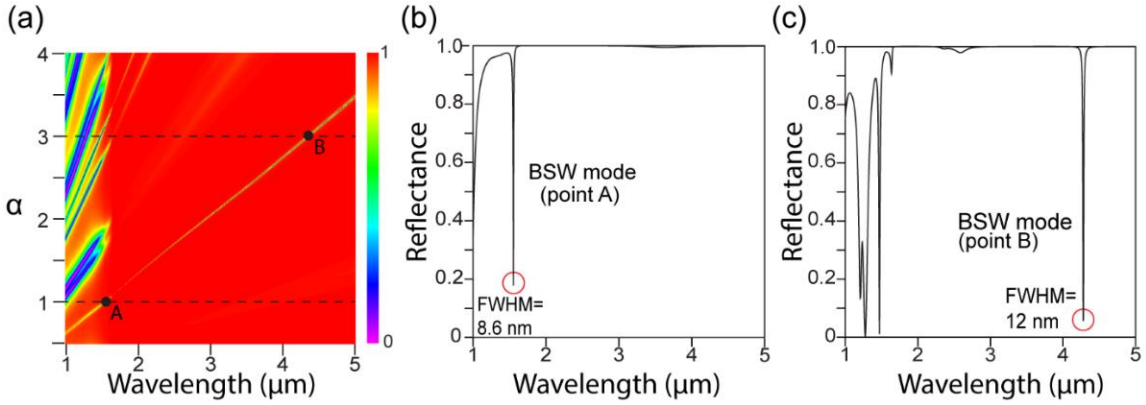

Figure 5-3 Reflectance variation as a function of thickness factor α and wavelength. The ratio of the Ge and SiO_2 thickness is fixed. Reflectance spectrum of the Ge/ SiO_2 multilayer for (b) α = 1 and (c) α = 3.

Figure 5-4 shows the simulated reflectance variation with the incident angle and wavelength for the TE-polarized incident light for the Ge/SiO_2 multilayer thickness with the case of α = 1. When the incident angle θ is larger than the critical angle for total reflection (44.6°), it is found that light is reflected except at specific wavelengths. These resonance wavelengths correspond to the BSWs, which are observed as a decrease in reflectance intensity when the surface modes are excited

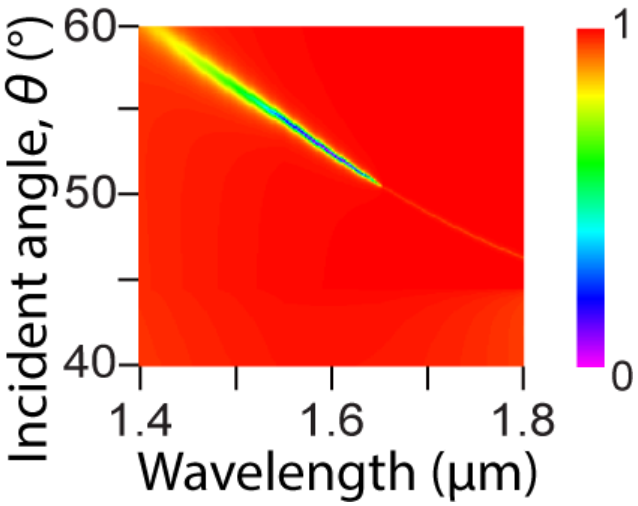

Figure 5-4 Reflectance variation of the two-pair Ge/SiO_2 BSW multilayer as a function of the incident angle θ and wavelength λ.

Noting that the Ge/SiO_2 multilayer realizes the strong BSW with only two pairs, while the reported BSW structures in the visible [26] and NIR [24,25,39,80,86–88] regions require more than six pairs to sustain strong BSW modes. The large difference between the refractive indices of Ge and SiO_2 and the small values of the extinction coefficient in the NIR to MIR regions make it possible for the Ge/SiO_2 multilayer to sustain BSW modes from the NIR to MIR regions with only two pairs. The simulated reflectance spectrum in the NIR region for BSW modes obtained with the widely used combination of materials consisting of alternating Si_3N_4 and SiO_2 layers as shown in Figure 5.4(a). In comparison to the proposed Ge/SiO_2 two-pair multilayer BSW platform exhibiting a reflectance of 0.18 at the BSW condition, the Si_3N_4/SiO_2 based BSW structure with two pairs, four pairs, and six pairs only achieve the reflectance dip values of 0.99, 0.89, and 0.69, respectively. These results indicate the weak coupling of light due to the small refractive index difference between Si_3N_4 and SiO_2. The thickness of the two-pair Si_3N_4/SiO_2 multilayer has been designed for coupling BSW mode in the MIR region as shown in Figure 5-4(b) In comparison, a low reflectance (0.18) and narrow bandwidth (FWHM = 12 nm) are achieved with Ge/SiO_2 two-pair multilayer. On the other hand,

The BSW mode obtained with the two-pair Si_3N_4/SiO_2 multilayer exhibits a reflectance of 0.78 and a larger FWHM of 125 nm. It is noted that the reflectance dips at the resonance wavelengths of the two-pair Ge/SiO_2 multilayer remain narrow in a wide range of wavelengths as shown in Figure5-4(c). In contrast, the reflectance dips at the resonance wavelength of the two-pair Si_3H_4/SiO_2 multilayer broadens with the increase of the wavelength.

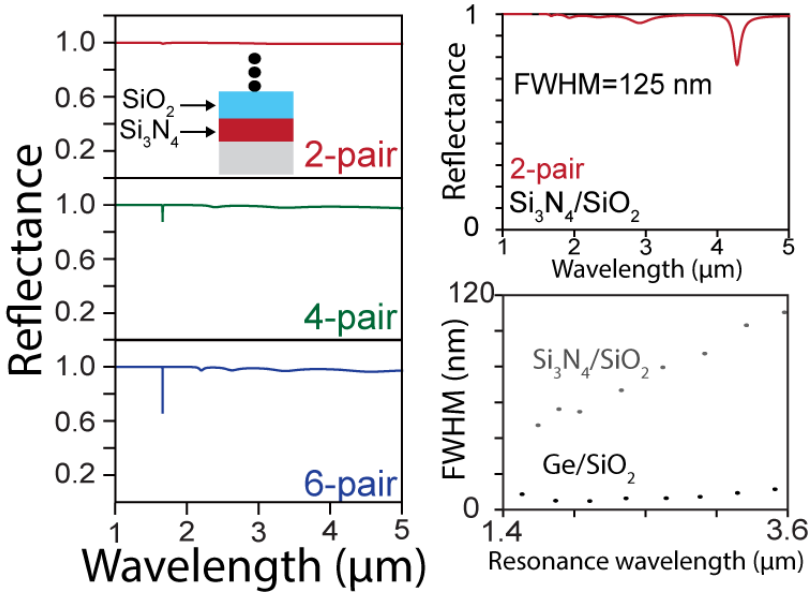

Figure 5-5 Reflectance spectrum of two-pair (red), four-pair (green), and six-pair (blue) Si_3N_4/SiO_2 BSW multilayers (b) Reflectance spectrum of the two-pair Si_3N_4 BSW multilayer in the MIR region (c) FWHM of the reflectance dip as a function of the resonance wavelength for the two-pair Ge/SiO_2 multilayer in the MIR region

To understand the behavior of the electric field of BSW mode, the 2D finite-difference time-domain (FDTD) simulations (FullWAVE, RSoft Design Group, Ossining, U.S.A) have been performed. Figure 5-5 shows the simulated electric field distribution for the BSW mode found in Ge/SiO_2 two-pair multilayer and Si_3H_4/SiO_2 two-pair multilayer both in NIR and MIR regions. The electric field distributions exhibit the evanescent decay of the field at the interface between the multilayer and air as shown in Figures 5-

6 (a) and (b). The maximum of the electric field corresponds to the top of the multilayer structure. Due to the smaller extinction of Ge in the MIR region, the electric field enhancement is even larger than that in the NIR region. As a result, the maximum electric field of the BSW mode for the Ge/SiO_2 two-pair multilayer is higher than that of the two-pair Si_3H_4/SiO_2 two-pair multilayer as shown in Figure 5-6 (c) and (d). Moreover, the Ge/SiO_2 two-pair multilayer requires only around half of the thickness to achieve the same BSW resonance wavelength compared to the two-pair Si_3H_4/SiO_2 multilayer.

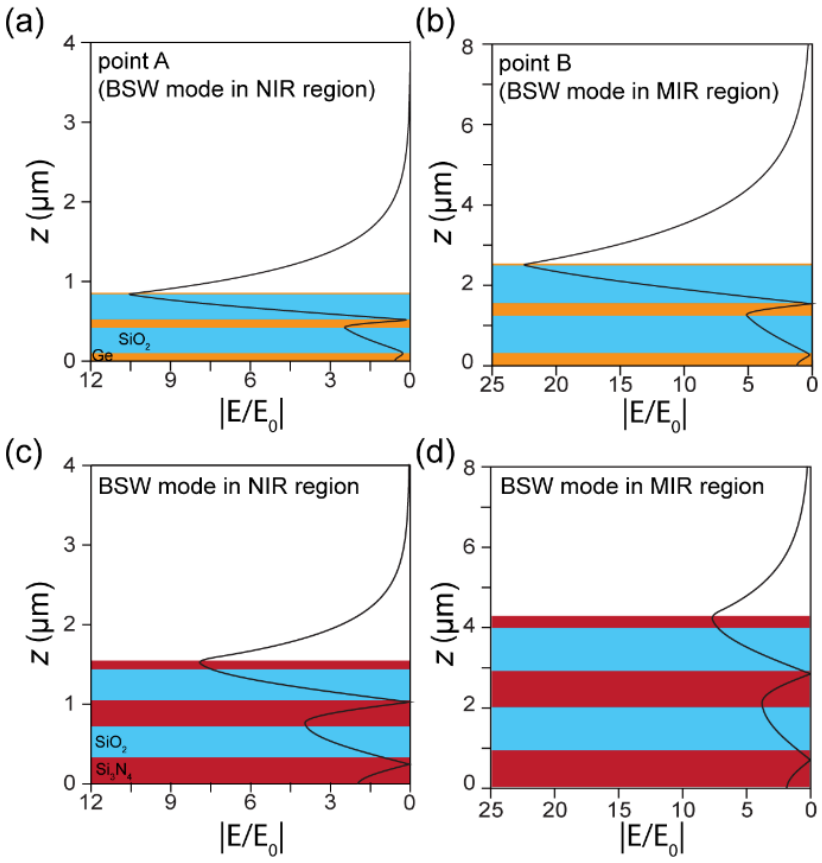

Figure 5-6 One-dimensional electric field distribution along the z-axis of the fundamental BSW mode for the two-pair Ge/SiO_2 in (a) NIR regions and (b) MIR region and Si_3N_4/SiO_2 BSW multilayer in (c) NIR region and (d) MIR region.

5.2 Prism coupling configuration surface wave measurement setup

The Ge/SiO_2 two-pair multilayer that can sustain BSW modes in NIR and MIR regions has been fabricated by using RF-magnetron sputtering system (CFS-4ES, Shibaura Engineering Works Co., Ltd., Yokohama, Japan). The scanning electron microscopy (SEM) image of the cross-section of the fabricated multilayer sustaining BSW in the NIR region is shown in Figure 5-7 (a). Figure 5-7 (b) shows the experimental setup used to measure the light reflectance of the Ge/SiO_2 two-pair multilayer. A halogen lamp was used as a light source to provide a wide range of wavelengths. A wire grid polarizer was placed in front of the sample to control the light polarization (TE or TM). The prism was placed on a θ-2θ rotation stage to realize angle-dependence measurements. A Fourier-transform infrared (FTIR) spectrometer equipped with a mercury cadmium telluride (MCT) detector was used to collect light reflected from the sample.

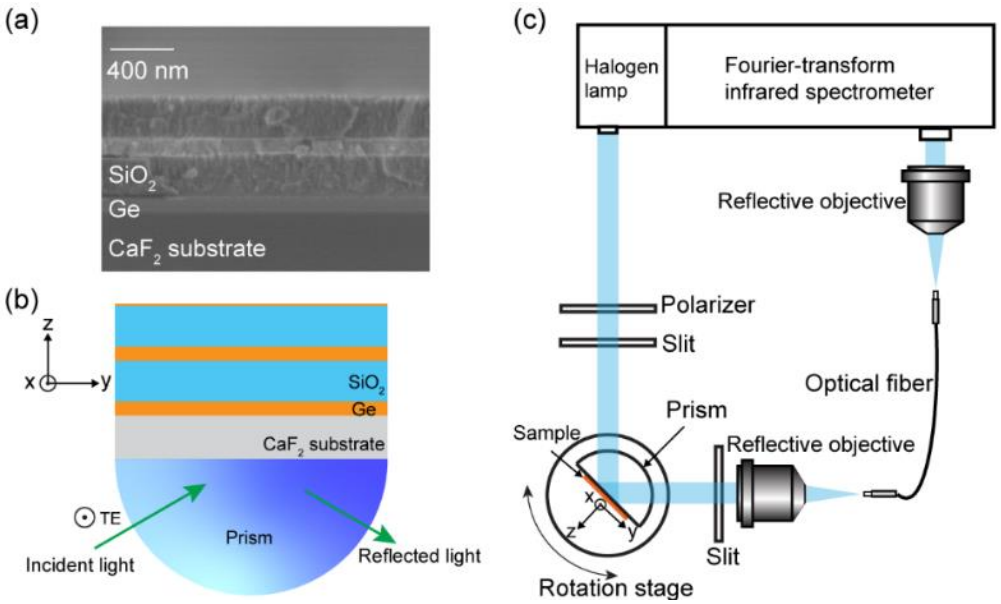

Figure 5-7 Schematic diagram of the measurement setup. (a) Scanning electron microscopy cross-sectional view of the two-pair Ge/SiO_2 BSW multilayer. (b) BSW mode couple by a prism (c) Light reflectance measurement setup used to characterize the angular dependency of the reflectance spectrum.

5.3 Demonstration of BSW both in NIR and MIR regions

Figure 5-8 shows the reflectance measurement results of the fabricated Ge/SiO_2 two-pair BSW multilayers for both cases $\alpha = 1$ and $\alpha = 3$ at different incident angles. The reflectance spectrum is shown in Figure 5-8(a) exhibits only one sharp dip (FWHM = 34 nm) corresponding to the fundamental BSW and showing good agreement with the simulation result of Figure 5.3. The difference in FWHM between the observed and computed results originated from the beam divergence induced by the finite size of the prism. With the help of ray tracing simulation, this beam divergence was estimated to be approximately 0.35°. Taking into account the beam divergence, we estimated by simulation the FWHM to be 24 nm (the computed FWHM was 8.6 nm without beam divergence). The observed FWHM was 34 nm, and so the beam divergence explained most of the difference between the observed and ideal FWHM. The inset shows the reflectance dip of the two-pair BSW multilayer in the MIR range. The reflectance dip positions for both $\alpha = 1$ and $\alpha = 3$ redshift with the decreasing incident angle as shown in Figure 5-8(b). The observed relation between the incident angle and the reflectance dip wavelength in the case $\alpha = 1$ is shown in Figure 5.7(c). It is noted that the trend of Figure 5-8(c) is similar to the simulated results of Figure 5.3. The difference between the simulated and experimental results is caused by the difference between the actual and the ideal refractive indices of Ge, as in the simulation, Ge is assumed to be a single crystal material and the deposited Ge layer should be amorphous. Figure 5-8 (d) shows the relation between the reflectance and the incident angle at the fixed wavelength of $\lambda = 1550$ nm. The observed FWHM of the dip is 0.88° and the computed FWHM is 0.36°. The difference between the observed and computed results is caused by beam divergence caused by the finite size of the prism as mentioned above; taking into

account the illumination beam divergence, we estimated by simulation the FWHM to be 0.85°.

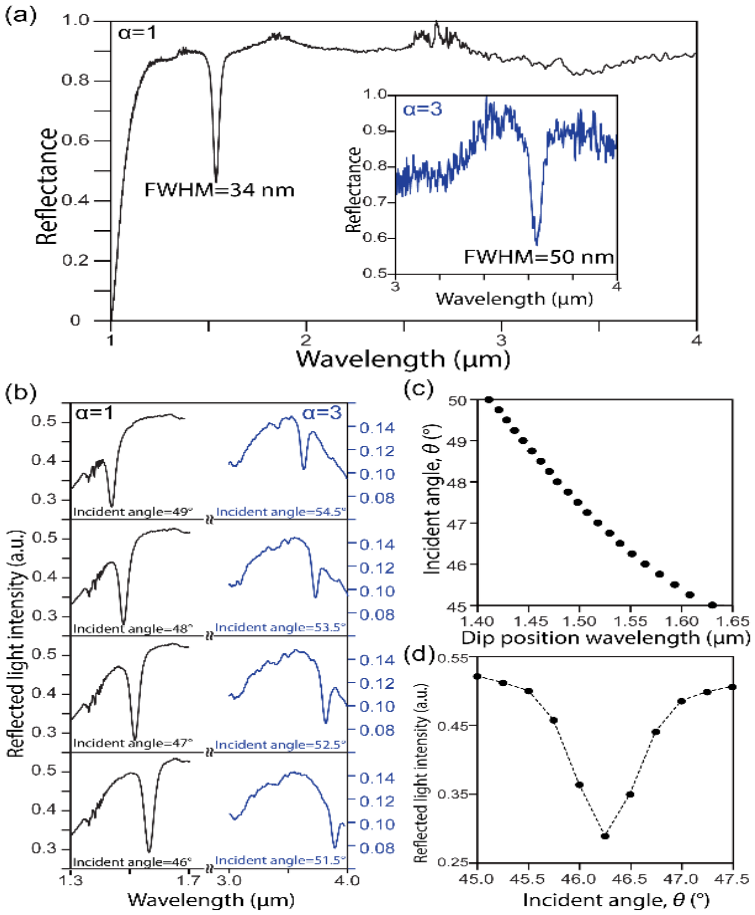

Figure 5-8 Measured reflectance spectra and angular dependence of the two-pair Ge/SiO_2 BSW multilayer. (a) The reflectance spectrum of the two-pair BSW multilayer. Inset: Reflectance spectrum of the two-pair BSW multilayer with the fundamental BSW mode designed in the MIR region. (b) Variation of the reflectance dip position with the incident light angle in the NIR range (black) and MIR range (blue). (c) Relation between the reflectance dip position and incident angle. (d) Angular dependence of reflectance at λ= 1550 nm

In order to observe the BSW on the top of the two-pair BSW multilayer, a different setup [Figure 5-9 (a)] is used. The tunable C- and L-band lasers and the NIR camera were used to capture the BSW propagating on the surface by detecting scattered light

from particles sitting on the BSW multilayer surface. The measurement results of the BSW detection for the two-pair BSW multilayer are shown in Figure 5-9(b). To improve the light collection by the NIR camera, the top surface of the structure is modified with Au nanoparticles so as to enhance the scattering of the propagating surface wave. By analyzing the intensity of the images collected with the NIR camera when the incident light was TE polarized, the scattered light intensity as a function of wavelength is obtained [black dots in Figure 5-9(b)]. The result for the TM-polarized light (gray dots) is shown in Figure 5-9(b) and exhibits no wavelength dependency in contrast to the result obtained with the TE-polarized light. This difference provides evidence for the excitation of the BSW mode for the incident TE-polarized light. In Figure 5-9(b), the intensity peak position shows good agreement with the reflectance dip. Figure 5-9(c) shows the intensity of the scattered light along the y-axis measured in the far-field with the NIR camera for the BSW having λ= 1551 nm. The observed intensity profile comprised a Gaussian component (laser beam width of 1.9 mm) and an exponential decay of the BSW [red curve in Figure 5-9(c)] with a propagation length of 200 μm. The simulation of the propagation length provided in Figure 5-9(c) gives a propagation length of approximately 250 μm, which is in good agreement with the experimental result. The observed propagation length is of the same order as those reported for the six-pair Si_3N_4/SiO_2 multilayer BSW platform [80] and the ten-pair hydrogenated amorphous SiNx multilayer BSW platform [24,89].

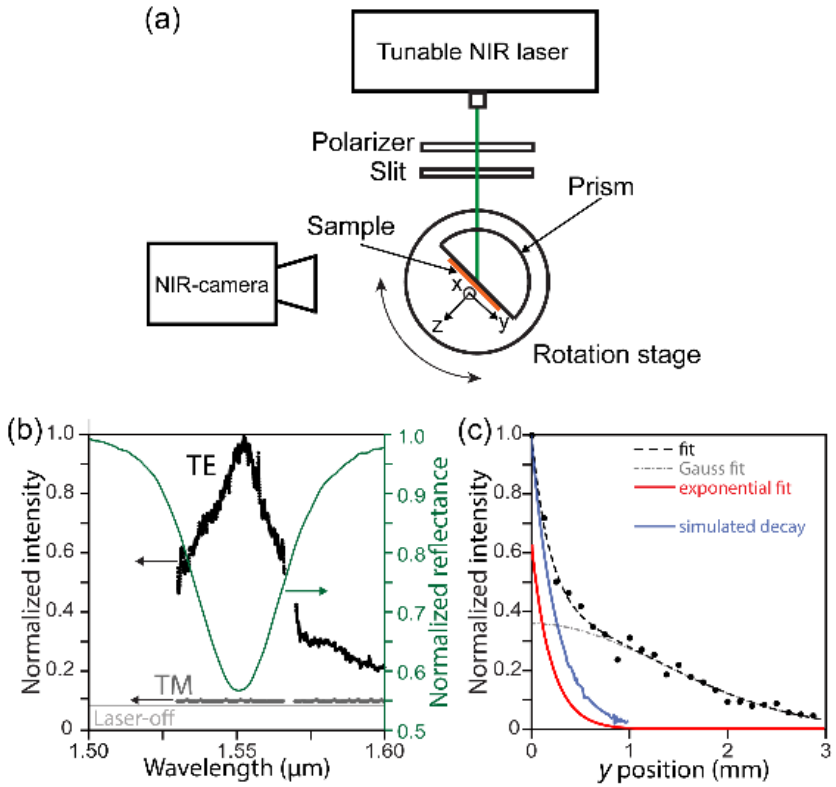

Figure 5-9 Characterization of BSW in the NIR range. (a) Surface wave measurement setup to demonstrate the direct observation of the BSW. (b) Variation of the surface wave intensity covering the C- and L-band wavelength range with TE (black) and TM (gray) polarized light together with the reflectance spectrum (green). (c) Variation of the scattered light intensity for TE polarization along the y-axis with the fitted curves, together with the simulated propagation decay.

5.4 Discussions

In summary, we experimentally demonstrated excitation of BSW with a multilayer consisting of two-pairs of Ge/SiO_2 layer. By exploiting the large refractive index difference between Ge and SiO_2, the BSW platform can be realized with only two pairs of alternating layers. In this way, the number of layers required for coupling a BSW mode is reduced drastically in comparison with the widely used alternating Si_3N_4/SiO_2 dielectric layers that require more than six pairs. Additionally, the required

total thickness for exciting the same BSW mode using the Ge/SiO_2 multilayer is reduced by approximately two times compared to the required total thickness of the Si_3N_4/SiO_2 multilayer. Moreover, BSW was experimentally demonstrated in the MIR range using the Ge/SiO_2 two-pair multilayer by tuning the thickness of the multilayer. The BSW mode was observed in the MIR range up to 4130 nm, thus greatly extending the range of BSW mode wavelengths beyond the NIR and possibly reaching the fingerprint region of organic molecules. Table 5.1 shows the demonstration of BSW in different wavelength regions with different materials. BSW has been extensively studied in Vis and NIR regions, but the number of pairs is usually larger than 4. One study exhibited the BSW in the MIR region, but the materials that are used for the BSW platform are not very common and practical [82]. In this work, BSWs have been demonstrated both in NIR and MIR regions with very common materials, Ge and SiO_2. Additionally, thanks to the large difference in the refractive index between Ge and SiO_2, 2-pairs multilayer is good enough for coupling BSW mode.

Table 5.1: Summary of the recent plain (no structure or pattern on top surface) BSW platform

Structure	**Number of pairs**	**Wavelength region**	**Propagation length (μm)**	
Si_3N_4/SiO_2 multilayer	4	Vis (0.63 μm)	NA	Paeder et al. *Sensor and Actuators B:Chemical*, (2017) [90]
SiN_x/SiO_2 multilayer	4	NIR region (1.55 μm)	3240 @ λ = 1.55 μm	Richa et al. *Journal of the European Optical Society-Rapid Publication*, (2018) [18]

Ge/ZnSe multilayer	7	NIR region (1.46 μm)	NA	Ma, j et al. *Optics letters*, (2018) [21]
$ZnSe/YBF_3$ multilayer	3	MIR region (7.6~8.1 μm)	NA	Smolik et al, *ACS Photonics*, (2018) [82]
Ge/SiO_2 multilayer	**2**	**From NIR to MIR regions (1~5 μm)**	**250 @ λ = 1.55 μm**	**Deng et al. Applied Physics Letters, (2020)**

Chapter 6 : Conclusions and Future work

References

[1] J. A. Polo and A. Lakhtakia, *Surface Electromagnetic Waves: A Review*, Laser Photonics Rev. **5**, 234 (2011).

[2] O. Takayama, A. A. Bogdanov, and A. V. Lavrinenko, *Photonic Surface Waves on Metamaterial Interfaces*, J. Phys. Condens. Matter **29**, (2017).

[3] H. Raether, *Surface Plasmons on Smooth Surfaces* (Springer, Berlin, Heidelberg, 1988).

[4] A. V. Zayats, I. I. Smolyaninov, and A. A. Maradudin, *Nano-Optics of Surface Plasmon Polaritons*, Phys. Rep. **408**, 131 (2005).

[5] B. D. Gupta, A. M. Shrivastav, and S. P. Usha, *Surface Plasmon Resonance-Based Fiber Optic Sensors Utilizing Molecular Imprinting*, Sensors (Switzerland) **16**, (2016).

[6] J. Homola, *Surface Plasmon Resonance Sensors for Detection of Chemical and Biological Species*, Chem. Rev. **108**, 462 (2008).

[7] J. Homola, *Present and Future of Surface Plasmon Resonance Biosensors*, Anal. Bioanal. Chem. **377**, 528 (2003).

[8] S. S. Yee and R. C. Jorgenson, *A Fiber Optic Chemical Sensor Based on Surface Plasmon Resonance*, Sensors Actuators B Chem. **12**, 213 (1993).

[9] C. T. Campbell and G. Kim, *SPR Microscopy and Its Applications to High-Throughput Analyses of Biomolecular Binding Events and Their Kinetics*, Biomaterials **28**, 2380 (2007).

[10] H. Wei and H. Xu, *Nanowire-Based Plasmonic Waveguides and Devices for Integrated Nanophotonic Circuits*, Nanophotonics **1**, 155 (2012).

[11] M. A. Otte, B. Sepúlveda, W. Ni, J. P. Juste, L. M. Liz-Marzán, and L. M. Lechuga, *Identification of the Optimal Spectral Region for Plasmonic and Nanoplasmonic Sensing*, ACS Nano **4**, 349 (2010).

[12] G. Bracher, K. Schraml, C. Jakubeit, M. Kaniber, and J. J. Finley, *Direct Measurement of Plasmon Propagation Lengths on Lithographically Defined Metallic Waveguides on GaAs*, J. Appl. Phys. **110**, (2011).

[13] P. Yeh, A. Yariv, and A. Y. Cho, *Optical Surface Waves in Periodic Layered Media*, Appl. Phys. Lett. **32**, 104 (1978).

[14] W. M. Robertson and M. S. May, *Surface Electromagnetic Wave Excitation on One-Dimensional Photonic Band-Gap Arrays*, Appl. Phys. Lett. **74**, 1800 (1999).

[15] N. Danz, A. Sinibaldi, F. Michelotti, E. Descrovi, P. Munzert, U. Schulz, and F. Sonntag, *Improving the Sensitivity of Optical Biosensors by Means of Bloch Surface Waves*, Biomed. Tech. **57**, 584 (2012).

[16] A. Sinibaldi, N. Danz, E. Descrovi, P. Munzert, U. Schulz, F. Sonntag, L. Dominici, and F. Michelotti, *Direct Comparison of the Performance of Bloch Surface Wave and Surface Plasmon Polariton Sensors*, Sensors Actuators, B Chem. **174**, 292 (2012).

[17] V. Koju and W. M. Robertson, *Excitation of Bloch-like Surface Waves in Quasi-Crystals and Aperiodic Dielectric Multilayers*, Opt. Lett. **41**, 2915 (2016).

[18] R. Dubey, E. Barakat, M. Häyrinen, M. Roussey, S. K. Honkanen, M. Kuittinen, and H. P. Herzig, *Experimental Investigation of the Propagation Properties of Bloch Surface Waves on Dielectric Multilayer Platform*, J. Eur. Opt. Soc. **13**, (2017).

[19] M. Menotti and M. Liscidini, *Optical Resonators Based on Bloch Surface Waves*, J. Opt. Soc. Am. B **32**, 431 (2015).

[20] C. Summonte, F. Giorgis, E. Descrovi, F. Michelotti, and L. Dominici, *Experimental Determination of the Sensitivity of Bloch Surface Waves Based Sensors*, Opt. Express **18**, 8087 (2010).

[21] Z. H. I. U. O. W. Ang, *Sensing Performance Optimization of the Bloch Surface Wave Biosensor Based on the Bloch Impedance-Matching Method*, **43**, 84 (2018).

[22] H. Qiao, B. Guan, J. J. Gooding, and P. J. Reece, *Protease Detection Using a Porous Silicon Based Bloch Surface Wave Optical Biosensor*, Opt. Express **18**, 15174 (2010).

[23] H. Herzig, M.-S. Kim, R. Dubey, B. Vosoughi Lahijani, M. Marchena, and V. Pruneri, *Bloch Surface Waves Using Graphene Layers: An Approach toward In-Plane Photodetectors*, Appl. Sci. **8**, 390 (2018).

[24] E. Descrovi, T. Sfez, M. Quaglio, D. Brunazzo, L. Dominici, F. Michelotti, H. P. Herzig, O. J. F. Martin, and F. Giorgis, *Guided Bloch Surface Waves on Ultrathin Polymeric Ridges*, Nano Lett. **10**, 2087 (2010).

[25] B. Vosoughi Lahijani, M. Kuittinen, R. Dubey, M. Häyrinen, H. P. Herzig, and M. Roussey, *Ultra-Thin Bloch-Surface-Wave-Based Reflector at Telecommunication Wavelength*, Photonics Res. **5**, 494 (2017).

[26] R. Wang, H. Xia, D. Zhang, J. Chen, L. Zhu, Y. Wang, E. Yang, T. Zang, X. Wen, G. Zou, P. Wang, H. Ming, R. Badugu, and J. R. Lakowicz, *Bloch Surface Waves Confined in One Dimension with a Single Polymeric Nanofibre*, Nat. Commun. **8**, 1 (2017).

[27] M. Ballarini, F. Frascella, E. Enrico, P. Mandracci, N. De Leo, F. Michelotti, F. Giorgis, and E. Descrovi, *Bloch Surface Waves-Controlled Fluorescence Emission: Coupling into Nanometer-Sized Polymeric Waveguides*, Appl. Phys. Lett. **100**, (2012).

[28] A. Phys, *Bloch Surface Wave Ring Resonator Based on Porous Silicon Bloch Surface Wave Ring Resonator Based on Porous Silicon*, **011101**, 1 (2019).

[29] K. R. Safronov, D. N. Gulkin, I. M. Antropov, K. A. Abrashitova, V. O. Bessonov, and A. A. Fedyanin, *Multimode Interference of Bloch Surface Electromagnetic Waves*, ACS Nano **14**, 10428 (2020).

[30] R. Wang, H. Xia, D. Zhang, J. Chen, L. Zhu, Y. Wang, E. Yang, T. Zang, X. Wen, G. Zou, P. Wang, H. Ming, R. Badugu, and J. R. Lakowicz, *Bloch Surface Waves Confined in One Dimension with a Single Polymeric Nanofibre*, Nat. Commun. **8**, (2017).

[31] G. M. Smolik, N. Descharmes, and H. P. Herzig, *Toward Bloch Surface Wave-Assisted Spectroscopy in the Mid-Infrared Region*, ACS Photonics **5**, 1164 (2018).

[32] D. A. B. Miller, *Optical Interconnects to Silicon CMOS*, Proc. IEEE 2002 Int. Interconnect Technol. Conf. IITC 2002 **6**, 95 (2002).

[33] D. A. B. Miller, *Rationale and Challenges for Optical Interconnects to Electronic Chips*, Proc. IEEE **88**, 728 (2000).

[34] D. A. B. Miller, *Device Requirements for Optical Interconnects to Silicon Chips*, Proc. IEEE **97**, 1166 (2009).

[35] M. Hochberg, T. Baehr-Jones, G. Wang, M. Shearn, K. Harvard, J. Luo, B. Chen, Z. Shi, R. Lawson, P. Sullivan, A. K. Y. Jen, L. Dalton, and A. Scherer, *Terahertz All-Optical Modulation in a Silicon-Polymer Hybrid System*, Nat. Mater. **5**, 703 (2006).

[36] C. P. T. McPolin, J. S. Bouillard, S. Vilain, A. V. Krasavin, W. Dickson, D. O'Connor, G. A. Wurtz, J. Justice, B. Corbett, and A. V. Zayats, *Integrated Plasmonic Circuitry on a Vertical-Cavity Surface-Emitting Semiconductor Laser Platform*, Nat. Commun. **7**, 1 (2016).

[37] C. Koos, P. Vorreau, T. Vallaitis, P. Dumon, W. Bogaerts, R. Baets, B. Esembeson, I. Biaggio, T. Michinobu, F. Diederich, W. Freude, and J. Leuthold, *All-Optical High-Speed Signal Processing with Silicon-Organic Hybrid Slot Waveguides*, Nat. Photonics **3**, 216 (2009).

[38] L. Zhuang, C. G. H. Roeloffzen, M. Hoekman, K.-J. Boller, and A. J. Lowery, *Programmable Photonic Signal Processor Chip for Radiofrequency Applications*, Optica **2**, 854 (2015).

[39] T. Kovalevich, P. Boyer, M. Suarez, R. Salut, M.-S. Kim, H. P. Herzig, M.-P. Bernal, and T. Grosjean, *Polarization Controlled Directional Propagation of Bloch Surface Wave*, Opt. Express **25**, 5710 (2017).

[40] T. Kovalevich, P. Boyer, M. Suarez, R. Salut, M.-S. Kim, H. P. Herzig, M.-P. Bernal, and T. Grosjean, *Polarization Controlled Directional Propagation of Bloch Surface Wave*, Opt. Express **25**, 5710 (2017).

[41] J. Lin, J. P. B. Mueller, Q. Wang, G. Yuan, N. Antoniou, X. C. Yuan, and F. Capasso, *Polarization-Controlled Tunable Directional Coupling of Surface Plasmon Polaritons*, Science (80-.). **340**, 331 (2013).

[42] J. Jin, X. Li, Y. Guo, M. Pu, P. Gao, X. Ma, and X. Luo, *Polarization-Controlled Unidirectional Excitation of Surface Plasmon Polaritons Utilizing Catenary Apertures*, Nanoscale **11**, 3855 (2019).

[43] L. Huang, X. Chen, B. Bai, Q. Tan, G. Jin, T. Zentgraf, and S. Zhang, *Helicity Dependent Directional Surface Plasmon Polariton Excitation Using a Metasurface with Interfacial Phase Discontinuity*, Light Sci. Appl. **2**, 1 (2013).

[44] H. Mühlenbernd, P. Georgi, N. Pholchai, L. Huang, G. Li, S. Zhang, and T. Zentgraf, *Amplitude- and Phase-Controlled Surface Plasmon Polariton Excitation with Metasurfaces*, ACS Photonics **3**, 124 (2016).

[45] C. Peng, J. Li, H. Liao, Z. Li, C. Sun, J. Chen, and Q. Gong, *Universal Linear-Optical Logic Gate with Maximal Intensity Contrast Ratios*, ACS Photonics **5**, 1137 (2018).

[46] A. E. Willner and S. Khaleghi, *All-Optical Signal Processing*, **32**, 660 (2014).

[47] D. G. S. Rao, S. Swarnakar, V. Palacharla, K. S. R. Raju, and S. Kumar, *Design of All-Optical AND, OR, and XOR Logic Gates Using Photonic Crystals for Switching Applications*, Photonic Netw. Commun. (2020).

[48] K. E. Stubkjaer, *Semiconductor Optical Amplifier-Based All-Optical Gates for High-Speed Optical Processing*, IEEE J. Sel. Top. Quantum Electron. **6**, 1428 (2000).

[49] Q. Liu and Z. B. Ouyang, *All-Optical Half Adder Based on Cross Structures in Two-Dimensional Photonic Crystals*, Guangzi Xuebao/Acta Photonica Sin. **37**, 46 (2008).

[50] F. Parandin and M. M. Karkhanehchi, *Terahertz All-Optical NOR and AND Logic Gates Based on 2D Photonic Crystals*, Superlattices Microstruct. **101**, 253 (2017).

[51] Z. Li, Z. Chen, and B. Li, *Optical Pulse Controlled All-Optical Logic Gates in SiGe/Si Multimode Interference*, Opt. Express **13**, 1033 (2005).

[52] Y. Fu, X. Hu, C. Lu, S. Yue, H. Yang, and Q. Gong, *All-Optical Logic Gates Based on Nanoscale Plasmonic Slot Waveguides*, Nano Lett. **12**, 5784 (2012).

[53] H. Wei, Z. Wang, X. Tian, M. Käll, and H. Xu, *Cascaded Logic Gates in Nanophotonic Plasmon Networks*, Nat. Commun. **2**, (2011).

[54] A. Sharaiha, J. Topomondzo, and P. Morel, *All-Optical Logic AND-NOR Gate with Three Inputs Based on Cross-Gain Modulation in a Semiconductor Optical Amplifier*, Opt. Commun. **265**, 322 (2006).

[55] D. I. Vulis, O. Reshef, P. Camayd-Munoz, and E. Mazur, *Manipulating the Flow of Light Using Dirac-Cone Zero-Index Metamaterials*, Reports Prog. Phys. **82**, (2019).

[56] X. Niu, X. Hu, S. Chu, and Q. Gong, *Epsilon-Near-Zero Photonics: A New Platform for Integrated Devices*, Adv. Opt. Mater. **6**, 1 (2018).

[57] A. Alù, M. G. Silveirinha, A. Salandrino, and N. Engheta, *Epsilon-near-Zero Metamaterials and Electromagnetic Sources: Tailoring the Radiation Phase Pattern*, Phys. Rev. B - Condens. Matter Mater. Phys. **75**, 1 (2007).

[58] S. Vassant, A. Archambault, F. Marquier, F. Pardo, U. Gennser, A. Cavanna, J. L. Pelouard, and J. J. Greffet, *Epsilon-near-Zero Mode for Active Optoelectronic Devices*, Phys. Rev. Lett. **109**, 1 (2012).

[59] D. A. I. V Ulis, Y. L. I. Ang, O. R. A. D. R. Eshef, and P. Hilip, *Monolithic CMOS-Compatible Zero-Index Metamaterials*, **25**, 2350 (2017).

[60] O. Reshef, P. Camayd-Muñoz, D. I. Vulis, Y. Li, M. Lončar, and E. Mazur, *Direct Observation of Phase-Free Propagation in a Silicon Waveguide*, ACS Photonics **4**, 2385 (2017).

[61] M. Minkov, I. A. D. Williamson, M. Xiao, and S. Fan, *Zero-Index Bound States in the Continuum*, Phys. Rev. Lett. **121**, 3 (2018).

[62] M. G. Silveirinha and N. Engheta, *Theory of Supercoupling, Squeezing Wave Energy, and Field Confinement in Narrow Channels and Tight Bends Using ε near-Zero Metamaterials*, Phys. Rev. B - Condens. Matter Mater. Phys. **76**, 1 (2007).

[63] V. Koju and W. M. Robertson, *Leaky Bloch-like Surface Waves in the Radiation-Continuum for Sensitivity Enhanced Biosensors via Azimuthal Interrogation*, Sci. Rep. **7**, 1 (2017).

[64] T. Kovalevich, D. Belharet, L. Robert, G. Ulliac, M.-S. Kim, H. P. Herzig, T. Grosjean, and M.-P. Bernal, *Bloch Surface Waves at the Telecommunication Wavelength with Lithium Niobate as the Top Layer for Integrated Optics*, Appl. Opt. **58**, 1757 (2019).

[65] M. Minkov, I. A. D. Williamson, M. Xiao, and S. Fan, *Zero-Index Bound States in the Continuum*, Phys. Rev. Lett. **121**, 2019 (2018).

[66] H. Alipour-Banaei, S. Serajmohammadi, and F. Mehdizadeh, *All Optical NAND Gate Based on Nonlinear Photonic Crystal Ring Resonators*, Optik (Stuttg). **130**, 1214 (2017).

[67] L. Fang, H.-Z. Luo, X.-P. Cao, S. Zheng, X.-L. Cai, and J. Wang, *Ultra-Directional High-Efficiency Chiral Silicon Photonic Circuits*, Optica **6**, 61 (2019).

[68] K. Y. Bliokh, F. J. Rodríguez-Fortuño, F. Nori, and A. V. Zayats, *Spin-Orbit Interactions of Light*, Nat. Photonics **9**, 796 (2015).

[69] K. Y. Bliokh, A. Y. Bekshaev, and F. Nori, *Extraordinary Momentum and Spin in Evanescent Waves*, Nat. Commun. **5**, 1 (2014).

[70] K. Y. Bliokh and F. Nori, *Transverse Spin of a Surface Polariton*, Phys. Rev. A - At. Mol. Opt. Phys. **85**, 1 (2012).

[71] F. J. Rodríguez-fortuño, A. Martínez, G. a Wurtz, and A. V Zayats, *Electromagnetic Guided Modes*, Science (80-.). **328**, 328 (2013).

[72] S. Y. Lee, I. M. Lee, J. Park, S. Oh, W. Lee, K. Y. Kim, and B. Lee, *Role of Magnetic Induction Currents in Nanoslit Excitation of Surface Plasmon Polaritons*, Phys. Rev. Lett. **108**, 1 (2012).

[73] Q. Jiang, Y. Bao, F. Lin, X. Zhu, S. Zhang, and Z. Fang, *Spin-Controlled Integrated Near- and Far-Field Optical Launcher*, Adv. Funct. Mater. **28**, 1 (2018).

[74] F. Ding and S. I. Bozhevolnyi, *A Review of Unidirectional Surface Plasmon Polariton Metacouplers*, IEEE J. Sel. Top. Quantum Electron. **25**, 1 (2019).

[75] A. Sinibaldi, N. Danz, E. Descrovi, P. Munzert, U. Schulz, F. Sonntag, L. Dominici, and F. Michelotti, *Direct Comparison of the Performance of Bloch Surface Wave and Surface Plasmon Polariton Sensors*, Sensors Actuators, B Chem. **174**, 292 (2012).

[76] E. Descrovi, T. Sfez, M. Quaglio, D. Brunazzo, L. Dominici, F. Michelotti, H. P. Herzig, O. J. F. Martin, and F. Giorgis, *Guided Bloch Surface Waves on Ultrathin Polymeric Ridges*, Nano Lett. **10**, 2087 (2010).

[77] K. Toma, E. Descrovi, M. Toma, M. Ballarini, P. Mandracci, F. Giorgis, A. Mateescu, U. Jonas, W. Knoll, and J. Dostálek, *Bloch Surface Wave-Enhanced Fluorescence Biosensor*, Biosens. Bioelectron. **43**, 108 (2013).

[78] M. Wang, H. Zhang, T. Kovalevich, R. Salut, M.-S. Kim, M. A. Suarez, M.-P. Bernal, H.-P. Herzig, H. Lu, and T. Grosjean, *Magnetic Spin–Orbit Interaction of Light*, Light Sci. Appl. **7**, 24 (2018).

[79] F. Feng, S.-B. Wei, L. Li, C.-J. Min, X.-C. Yuan, and M. Somekh, *Spin-Orbit Coupling Controlled near-Field Propagation and Focusing of Bloch Surface Wave*, Opt. Express **27**, 27536 (2019).

[80] L. Yu, E. Barakat, T. Sfez, L. Hvozdara, J. Di Francesco, and H. P. Herzig, *Manipulating Bloch Surface Waves in 2D: A Platform Concept-Based Flat Lens*, Light Sci. Appl. **3**, (2014).

[81] T. Kovalevich, P. Boyer, M. Suarez, R. Salut, M.-S. Kim, H. P. Herzig, M.-P. Bernal, and T. Grosjean, *Polarization Controlled Directional Propagation of Bloch Surface Wave.*, Opt. Express **25**, 5710 (2017).

[82] G. M. Smolik, N. Descharmes, and H. P. Herzig, *Toward Bloch Surface Wave-Assisted Spectroscopy in the Mid-Infrared Region*, ACS Photonics **5**, 1164 (2018).

[83] P. T. Lin, S. W. Kwok, H. Y. G. Lin, V. Singh, L. C. Kimerling, G. M. Whitesides, and A. Agarwal, *Mid-Infrared Spectrometer Using Opto-Nanofluidic Slot-Waveguide for Label-Free on-Chip Chemical Sensing*, Nano Lett. **14**, 231 (2014).

[84] S. Romano, A. A. Lerman, V. N. Ionov, V. V. Sokolov, V. G. Artioushenko, G. A. Frank, W. Neuberger, V. S. Letohov, E. F. Kuzin, N. I. Afanasyeva, and A. P. Kryukov, *<title>MIR Fiber Spectroscopy for Minimal Invasive Diagnostics</Title>*, Med. Fiber Opt. Sensors Deliv. Syst. **2631**, 92 (2004).

[85] R. H. Wilson and H. S. Tapp, *Mid-Infrared Spectroscopy for Food Analysis: Recent New Applications and Relevant Developments in Sample Presentation Methods*, TrAC - Trends Anal. Chem. **18**, 85 (1999).

[86] F. Giorgis, E. Descrovi, C. Summonte, L. Dominici, and F. Michelotti, *Experimental Determination of the Sensitivity of Bloch Surface Waves Based Sensors*, Opt. Express **18**, 8087 (2010).

[87] J. Ma, X.-B. Kang, and Z.-G. Wang, *Sensing Performance Optimization of the Bloch Surface Wave Biosensor Based on the Bloch Impedance-Matching Method*, Opt. Lett. **43**, 5375 (2018).

[88] R. Dubey, M. Marchena, B. Vosoughi Lahijani, M.-S. Kim, V. Pruneri, and H. Herzig, *Bloch Surface Waves Using Graphene Layers: An Approach toward In-Plane Photodetectors*, Appl. Sci. **8**, 390 (2018).

[89] O. J. F. Martin, D. Brunazzo, H. P. Herzig, L. Dominici, M. Quaglio, E. Descrovi, F. Michelotti, F. Giorgis, L. Yu, W. Nakagawa, and T. Sfez, *Bloch Surface Waves in Ultrathin Waveguides: Near-Field Investigation of Mode Polarization and Propagation*, J. Opt. Soc. Am. B **27**, 1617 (2010).

[90] W. Kong, Z. Zheng, Y. Wan, S. Li, and J. Liu, *High-Sensitivity Sensing Based on Intensity-Interrogated Bloch Surface Wave Sensors*, Sensors Actuators, B Chem. **193**, 467 (2014).